# Entropy generation and exergy destruction in condensing steam flow through turbine blade with surface roughness

Hongbing Ding[1], Yiming Li[1], Esmail Lakzian[2], Chuang Wen[3], Chao Wang[1, *]

[1]Tianjin Key Laboratory of Process Measurement and Control, School of Electrical and Information Engineering, Tianjin University, Tianjin 300072, China

[2]Department of Mechanical Engineering, Hakim Sabzevari University, Sabzevar, Iran

[3]Faculty of Engineering, University of Nottingham, University Park, Nottingham NG7 2RD, UK

*Corresponding author: Chao Wang, Email: wangchao@tju.edu.cn

**Abstract:** In the steam turbine, the wetness loss due to vapor condensation is one of the most crucial losses at low-pressure stage. This study focused on entropy generation and exergy destruction of condensing steam flow in turbine blade with the roughness. The governing equations including entropy transport equation combined with condensation model, transition SST model and roughness correlation_were established and verified by experiments and theory. Flow field behaviors, such as wetness fraction, intermittency and turbulent viscosity distributions, controlled by the deviation angle were obtained to evaluate effects of back pressure ratio and surface roughness. The mass-averaged wetness fraction at outlet was also extracted considering the influence of uneven mass flux. Finally, each part of entropy generation derived from viscous, heat conduction, phase change and aerodynamic losses and exergy destruction ratio were analyzed. Research shows that roughness plays an important part in the intermittency and turbulent viscosity. The mass-averaged wetness fraction at outlet sharply drops with back pressure ratio but slightly decreases with the roughness. With the roughness rising

or back pressure dropping, the entropy generation grows resulting in more exergy destruction. The maximum value of the total entropy generation is 84.520 J·kg$^{-1}$·K$^{-1}$, corresponding exergy destruction is 25.187 kJ·kg$^{-1}$ and exergy destruction ratio is 4.43%.

**Keywords**: Steam turbine; Non-equilibrium condensation; Entropy generation; Exergy destruction; Transition SST model; Surface roughness

**Nomenclature**

| | | | |
|---|---|---|---|
| $A$ | area, m$^2$ | | intermittency, - |
| $c_p$ | specific heat capacity, J·kg$^{-1}$·K | $_v$ | specific heat ratio, - |
| $d$ | diameter of turbine throat, m | $T$ | subcooling, $T_{sat}(p)$-$T_v$, K |
| $E$ | total energy, J·kg$^{-1}$ | $\delta_{ij}$ | Kronecker delta function |
| $e_x$ | specific exergy, J·kg$^{-1}$ | $\delta_1$ | displacement thickness, m |
| $G_k$, $G$ | generations due to mean velocity gradients | $\varepsilon$ | dissipation rate, m$^2$ s$^{-3}$ |
| $h$ | static enthalpy, J·kg$^{-1}$ | $\zeta$ | exergy destruction ratio, - |
| $h_{lv}$ | latent heat, J·kg$^{-1}$ | $\eta_{Loss}$ | performance loss coefficient, - |
| $I$ | nucleation rate, m$^{-3}$·s$^{-1}$ | $\theta$ | Kantrowitz correction coefficient, - |
| $K_s$ | average height of sand-grain roughness, m | | isentropic exponent, - |
| $K_b$ | Boltzmann's constant. 1.38×10$^{-23}$ J·K$^{-1}$ | $\lambda$ | thermal conductivity, W·m$^{-1}$·K$^{-1}$ |

| | | | |
|---|---|---|---|
| $k$ | turbulence kinetic energy, J·kg$^{-1}$ | $\mu$ | dynamic viscosity, Pa·s |
| $Ma$ | Mach number, - | $\mu_t$ | turbulent viscosity, Pa·s |
| $m_m$ | mass of water molecule, 2.99×10$^{-26}$ kg | $\rho$ | mixture density, kg·m$^{-3}$ |
| $n_p$ | the droplet number density, kg$^{-1}$ | | liquid surface tension, N·m$^{-1}$ |
| $Pr$ | Prandtl number, = $\mu c_p/\lambda$ | $_k$, | turbulent Prandtl number for $k$ and , - |
| $p$ | pressure, Pa | $_{i,j}$ | deviatoric stress tensor, Pa |
| $q_c$ | condensation coefficient, - | $\tau_w$ | wall shear stress, Pa |
| $q_m$ | mass flow-rate of wet steam, kg·s$^{-1}$ | ν | kinematic viscosity, m$^2$·s$^{-1}$ |
| $R_c$ | radius of the wall curvature, m | Φ | dissipation functions, W·m$^{-3}$ |
| $Re_{\theta t}$ | local transition momentum thickness Reynolds number, - | $\varphi$ | deviation angle, = -arctan($u$/$v$) |
| $R_v$ | specific vapor constant, J·kg$^{-1}$·K$^{-1}$ | $\phi$ | Mass flux, kg m$^{-2}$·s$^{-1}$ |
| $r$ | droplet radius, m | Ω | strain rate magnitude, s$^{-1}$ |
| $r^*$ | critical radius, m | $\omega$ | specific dissipation rate, s$^{-1}$ |
| $S$ | supersaturation ratio, - | *Subscripts* | |
| $S_{i,j}$ | the mean strain rate, m·s$^{-2}$ | 0 | the dead (environment) state |
| $s$ | specific entropy, J·kg$^{-1}$·K$^{-1}$ | eff | effective |
| $T$ | temperature, K | $d$ | destruction |
| $T_{sat}$ | saturation temperature, K | gen | entropy generation |
| $Tu$ | turbulence intensity, - | in, out | inlet, outlet |
| $t$ | time, s | $i$, $j$ | tensor notation |

| | | | |
|---|---|---|---|
| $U$ | local velocity, m·s$^{-1}$ | *is* | isentropic |
| $u_1$ | local freestream velocity, m·s$^{-1}$ | *l* | liquid |
| $u$, $v$, $w$ | velocity magnitude, m·s$^{-1}$ | *mix* | mixture |
| $u_\tau$, $u^*$ | the friction velocity, m·s$^{-1}$ | *ref* | reference |
| $V_d$ | droplet volume, m$^3$ | *sat* | saturation |
| $x$, $y$, $z$ | cartesian coordinates | *t* | turbulence |
| $Y_\phi$ | entropy generation rate, J K$^{-1}$·m$^{-3}$·s$^{-1}$ | *tran* | entropy transfer |
| $y^+$ | wall yplus | *v* | vapor |
| $Y_k$, $Y$ | dissipations of $k$ and due to turbulent | Superscripts | |
| *Greek* | | - | Time-averaged |
| $\alpha$ | Thermal diffusivity, = $\lambda/\rho c_p$, m$^2$·s$^{-1}$ | $'$ | fluctuation |
| $\beta$ | liquid mass (wetness) fraction, - | * | at stagnation condition |
| | mass generation rate, kg·m$^{-3}$·s$^{-1}$ | | |

## 1. Introduction

The steam turbine is an essential part of power generation plant for thermal and nuclear electric generation [1]. When the steam flow expands in turbine blade, it easily leads to the non-equilibrium condensation phenomena [2]. The existence of lots of droplets will result in blade erosion and reduce the efficiency of the steam turbine [3]. The heat transfer between vapor and liquid phase results in irreversibility [4] and the entropy generation is as a measurement of the system irreversibility [5]. Additionally, the surface roughness of the turbine blades resulted from thermal erosion, fouling and collision of particles also brings efficiency loss to steam turbine [6]. Therefore, it is necessary to develop the research for condensing steam flow through turbine blade.

Recently, improving efficiency of engineering system is more and more crucial due to the resource scarcity and economy development. The minimization of entropy is a method to design the efficient energy system. Many researchers have concentrated on the study of entropy generation in various turbine blades. Young [7] described a method to compute the total entropy generation of wet steam for turbine cascades. Eulerian and Lagrangian reference frame are respectively for the mixture conservation equations and nucleation and growth of water droplets solving. Bakhtar [8] compared the Runge-Kutta time-marching numerical scheme with the earlier Denton’s scheme, and the specific entropy and loss are estimated According to the study of Shehata [9] and Li [10] for Wells turbine blades and hydro-turbines performance, the result of entropy generation theory is better than that of earlier method such as the first law of thermodynamics. Thus, it is worthy to conduct the performance analysis and improvement based on both local and global entropy generation. Haseli [11] introduced specific entropy generation to improve thermal efficiency of power generating systems. From the discussion for a regenerative gas turbine, it is shown that with specific entropy generation decreasing, thermal efficiency increases. To optimize the operation of the geothermal power plant, Peña-Lamas [12] developed the correlations for the enthalpy and entropy to obtain the pressure and temperature of the turbine. Results showed that the method is more applicable compared with other technologies. Ghisu [13] calculated the entropy generation in Wells turbines concentrating on the effect of turbulent fluctuations and Reynolds averaging. It is demonstrated that the method can contribute to analyze and optimize the Wells turbines. Rajabi [14] studied the local and global entropy generation of different types and focused on the impact of the swirl number. The method is helpful to judge the disadvantage of the combustor. The entropy generation in condensation flow has also caused attention of researchers. For wet steam flow, Dykas [15] used entropy loss efficiency to estimate the losses. But the losses value was overestimated due to the neglect of the wetness fraction. By the numerical investigation of Bagheri-Esfe [16] and Vatanmakan [17] for the condensing steam flow through turbine blades, it is shown that the entropy generation induced by non-equilibrium condensation can reduce the steam turbine efficiency and the large heat flux can reduce entropy generation.

Exergy destruction is proportional to the entropy generation of the process [18]. It is not only a way to understand energy utilization quality, but also a method to analyze and optimize the thermal systems [19]. On the basis of the exergy analysis method, Voldsund [5] presented the comparison of the oil with gas processing plants and identified the origin of exergy destruction, providing guidance for the improvement of the system. Vučković [20] used the first and second level of exergy destruction splitting for the boiler to analyze an industrial plant and found there is potential exergy destruction that can be avoided. The conclusion is valuable to improve the boiler performance. Zhao [21] investigated the thermoelectric generation performance and found that humidification does lead to exergy destruction but has no effect on the energy. Chen [22] calculated and compared the exergy destruction of each components in heat-driven turbine by numerical simulation. Among several sources, the phase change and heat transfer are the main ones that cause exergy loss. Thus the optimization of heat transfer areas is needed.

Besides, the effects of surface roughness should be also considered when estimating the components performance losses. In 1996, Kind [23] found that surface roughness can give rise to more increment in profile losses but relatively little increment in pressure loss. Boyle [24] and Bai [25] analyzed the aerodynamic losses of turbine vanes caused by surface roughness for different Reynolds numbers while Zhang [26] mainly focused on the different Mach number distributions. The results showed the aerodynamic losses generally increase with higher Reynolds and Mach number. For the low pressure turbine, Montomoli [27] and Vazquez [28] concluded by experiments that the pressure losses will not increase when the blade is with as-cast roughness, but will increase total efficiency [29]. The surface roughness is also found having impact on nucleation sites and condensation film occurrence [30]. Esfe [31] numerically investigated the impacts of surface roughness on turbines performance with different Mach numbers. The pressure losses increase more significantly with Mach number increasing in wet steam flow compared with in dry steam flow. The values of both perform losses and pressure losses in wet steam flow are larger than those in dry condition. The influence of surface roughness is more significant in subsonic region.

However, few researchers have analyzed the various types of entropy generation and its exergy destruction of wet steam in the turbine blade considering the effects of the surface roughness and operation back pressure. Thus, in our study, the compressible RANS equations including entropy transport equation combining with condensation model, transition SST model and roughness correlation were built. Then, the flow field behaviors and the contribution of each part of entropy generation were extracted. Finally, the mass-averaged energy generation, the performance loss coefficient and exergy destruction ratio were analyzed and discussed.

## 2. CFD model

The CFD model of wet steam flow is built based on the following assumptions: The condensation is homogeneous. The droplet is spherical and has the same mean radius. The volume of the droplet phase and velocity slip between the vapor and droplet phases are negligible because the typical size of condensing droplet size is submicron. The released latent heat is completely absorbed by the vapor phase because the heat capacity of droplet is quite small.

### *2.1. Governing equations*

The conservation equations of vapor and liquid phases for compressible non-equilibrium condensing flow in tensor form are expressed as

$$\frac{\partial \rho}{\partial t}+\frac{\partial}{\partial x_i}\left(\rho \bar{u}_i\right)=0 \tag{1}$$

where $\bar{u}_i$ is the mean velocity component. The mixture properties are correrlated with vapor and liquid properties by the wetness factor $\beta$.

$$\frac{\partial \rho \bar{u}_i}{\partial t}+\frac{\partial}{\partial x_j}\left(\rho \bar{u}_i \bar{u}_j\right)=-\frac{\partial p}{\partial x_i}+\frac{\partial}{\partial x_j}\left[\mu\left(\frac{\partial \bar{u}_j}{\partial x_i}+\frac{\partial \bar{u}_i}{\partial x_j}-\frac{2}{3}\delta_{ij}\frac{\partial \bar{u}_l}{\partial x_l}\right)\right]+\frac{\partial}{\partial x_j}\left(-\rho \overline{u_i' u_j'}\right) \tag{2}$$

where $p$ is the fluid pressure, $\mu$ is the dynamic viscosity of the fluid, $\delta_{ij}$ is the Kronecker delta, and $u_i'$ is the fluctuating component of the fluid velocity.

$$\frac{\partial \rho E}{\partial t}+\frac{\partial}{\partial x_i}\left[\bar{u}_i\left(\rho E+p\right)\right]=\frac{\partial}{\partial x_j}\left[\left(\lambda+\frac{c_p \mu_t}{Pr_t}\right)\frac{\partial T}{\partial x_j}+u_i\left(\tau_{ij}\right)_{eff}\right] \tag{3}$$

where $E=h-\frac{p}{\rho}+\frac{1}{2}\left(\bar{u}^2+\bar{v}^2+\bar{w}^2\right)$ and $\left(\tau_{ij}\right)_{eff}$ is defined as

$$\left(\tau_{ij}\right)_{eff}=\left(\frac{\partial \bar{u}_j}{\partial x_i}+\frac{\partial \bar{u}_i}{\partial x_j}\right)-\frac{2}{3}\mu_{eff}\frac{\partial \bar{u}_l}{\partial x_l}\delta_{ij} \tag{4}$$

where $\mu_{eff}=\mu+\mu_t$ and the turbulent viscosity $\mu_t$ is computed by

$$\mu_t = \frac{\rho k}{\omega} \frac{1}{\max\left[\frac{1}{\alpha^*}, \frac{\Omega F_2}{a_1 \omega}\right]} \tag{5}$$

where $\Omega = \sqrt{2S_{i,j}S_{i,j}}$ .

Another two transport equations for $\beta$ and the droplets number $n_p$ in unit volume are

$$\frac{\partial \rho \beta}{\partial t} + \frac{\partial}{\partial x_i}\left(\rho u_i \beta\right) = \Gamma \tag{6}$$

$$\frac{\partial \rho n_p}{\partial t} + \frac{\partial}{\partial x_i}\left(\rho u_i n_p\right) = I \tag{7}$$

where $n_p$ is

$$n_p = \frac{\beta}{(1-\beta) V_d \left(\rho_l / \rho_v\right)} \tag{8}$$

The average droplet volume is

$$V_d = \frac{4}{3}\pi \bar{r}^3 \tag{9}$$

*2.2. Nucleation rate and droplet growth model*

The classic homogeneous nucleation rate which is the droplet generation rate with critical radius of the supercooled vapor is given by [32]

$$I = \frac{q_c}{1+\theta}\left(\frac{2\sigma}{\pi m_m^3}\right)^{1/2} \frac{\rho_v^2}{\rho_l} \exp\left(-\frac{4\pi r^{*2}\sigma}{3K_b T_v}\right) \tag{10}$$

where $q_c = 1$. The Kantrowitz correction $\theta$ is expressed as

$$\theta = 2\frac{\gamma_v - 1}{\gamma_v + 1}\frac{h_{lv}}{R_v T_c}\left(\frac{h_{lv}}{R_v T_v} - \frac{1}{2}\right) \tag{11}$$

where $h_{lv}$ is the specific enthalpy of evaporation, namely the latent heat of the condensation. The liquid surface tension $\sigma$ is

$$\sigma = a_1 \left( \frac{T_c - T}{T_c} \right)^{a_2} \left[ 1 + a_3 \left( \frac{T_c - T}{T_c} \right) \right] \tag{12}$$

where $a_1$ = 0.2358 N·m$^{-1}$, $a_2$ = 1.256, $a_3$ = -0.625, and $T_c$ =647.15 K.

The mass generation rate is computed by

$$\Gamma = \frac{4}{3}\pi\rho_l I r^{*3} + 4\pi\rho_l n_p \bar{r}^{-2} \frac{\partial \bar{r}}{\partial t} \tag{13}$$

$$r^* = \frac{2\sigma}{\rho_l R_v T_v \ln S} \tag{14}$$

where $S$ is the supersaturation ratio defined as the ratio of vapor pressure to saturation pressure. The growth rate of the droplet is

$$\frac{\partial \bar{r}}{\partial t} = \frac{p}{h_{lv}\rho_l \sqrt{2\pi R_v T_v}} \frac{\gamma + 1}{2\gamma} c_p \left( T_l - T_v \right) \tag{15}$$

where the droplet surface temperature $T_d$ is calculated by

$$T_l = T_{sat}\left( p \right) - \Delta T \frac{r^*}{r} \tag{16}$$

*2.3. Transition SST model*

Transition SST model is used to model the turbulence of the condensing flow. The turbulence kinetic energy $k$ and the specific dissipation rate are as follows:

$$\begin{aligned} &\frac{\partial}{\partial t}(\rho k) + \frac{\partial}{\partial x_i}(\rho k u_i) = \frac{\partial}{\partial x_j}\left[ \left( \mu + \frac{\mu_t}{\sigma_k} \right) \frac{\partial k}{\partial x_j} \right] + G_k - Y_k \\ &\frac{\partial \omega}{\partial t} + \frac{\partial}{\partial x_i}(\rho \omega u_i) = \frac{\partial}{\partial x_j}\left[ \left( \mu + \frac{\mu_t}{\sigma_\omega} \right) \frac{\partial \omega}{\partial x_j} \right] + G_\omega - Y_\omega + D_\omega \end{aligned} \tag{17}$$

The transport equation for the intermittency $\gamma$ is defined as

$$\frac{\partial(\rho\gamma)}{\partial t} + \frac{\partial(\rho u_j \gamma)}{\partial x_j} = P_{\gamma 1} - E_{\gamma 1} + P_{\gamma 2} - E_{\gamma 2} + \frac{\partial}{\partial x_j}\left[ \left( \mu + \frac{\mu_t}{\sigma_\gamma} \right) \frac{\partial \gamma}{\partial x_j} \right] \tag{18}$$

where $P$ , $E$ , $P$ , $E$ are transition sources. $\sigma_\gamma$ =1.0.

The transport equation for the transition momentum thickness Reynolds number

$Re_{\theta t}$ is

$$\frac{\partial\left(\rho Re_{\theta t}\right)}{\partial t}+\frac{\partial\left(\rho u_j Re_{\theta t}\right)}{\partial x_j}=P_{\theta t}+\frac{\partial}{\partial x_j}\left[\sigma_{\theta t}\left(\mu+\mu_t\right)\frac{\partial Re_{\theta t}}{\partial x_j}\right] \tag{19}$$

where $P_{\theta t}$ is the source term.

*2.4. Surface roughness correlation*

Considering the wall roughness has influence on the transition process, the empirical correlation for the transition momentum thickness Reynolds number has been defined as [33]

$$Re_{\theta t,\mathrm{rough}}=\begin{cases} Re_{\theta t} \\ \left(1/Re_{\theta t}+0.0061 f_{\Lambda}\left(K_s/\delta_1-0.01\right)^{f_{Tu}}\right)^{-1} \end{cases} \tag{20}$$

where $K_s$ is the average height of sand-grain roughness element, and $\delta_1$ is the displacement thickness.

For the automatic wall treatment of $k$-$\omega$ equations, the wall shear stress $\tau_w$ as a boundary condition is calculated as $\tau_w=\rho u^* u_\tau$, where two friction velocities $u^*$ and $u_\tau$ are blended between the viscous sublayer and the logarithmic region. The friction velocity $u^*$ is expressed by

$$u^*=\left(\frac{\nu u_p}{y_p}+C_\mu^{1/4}k\right)^{1/2} \tag{21}$$

where $y_p$ is the distance from point $P$ (wall-adjacent cell centroid) to the wall, $C_\mu$ is 0.09 and $\nu$ is kinematic viscosity. The friction velocity $u_\tau$ is

$$u_\tau=u_p\left[\left(y^+\right)^{-4}+\left(\frac{1}{\kappa}\ln\left(Ey^+\right)+\Delta B\right)^{-4}\right]^{1/4} \tag{22}$$

where $\kappa$ = 0.4187, $E$= 9.793 and $\Delta B$ is the roughness correction. For avoiding a singularity for large roughness heights, virtually the wall is shifted to 50% of the height of the roughness elements and the corrected value for $y^+$ of first cell center is $y^+ = y^+ + K_s^+/2$ , where the dimensionless parameter $y^+ = \sqrt{\tau_w/\rho}\, y_p/\nu$ and $K_s^+ = \sqrt{\tau_w/\rho} K_s/\nu$ . The values of $\Delta B$ in the hydro-dynamically smooth, transitional and fully rough regimes are calculated by

$$\Delta B = \begin{cases} 0, \quad K_s^+ < 2.25 \\ \dfrac{1}{\kappa}\ln\left[\dfrac{K_s^+ - 2.25}{87.75} + C_s K_s^+\right]\sin\left[0.4258\left(\ln K_s^+ - 0.811\right)\right], \; 2.25 \le K_s^+ \le 90 \\ \dfrac{1}{\kappa}\ln\left(1 + C_s K_s^+\right), \quad K_s^+ \ge 90 \end{cases} \tag{23}$$

where $C_S$ is a roughness constant of 0.5. The boundary conditions at the wall boundary are $\partial k/\partial n = 0$ and $\partial \omega/\partial n = 0$ , where $n$ is normal to the boundary. $\omega$ at wall is $\omega_w = \left(\omega_{vis}^2\left(y^+\right) + \omega_{\log}^2\left(y^+\right)\right)^{1/2}$, where $\omega_{vis}$ and $\omega_{\log}$ are the values of friction velocity in the linear and the logarithmic near-wall region that can be computed by $\omega_{vis} = 6\Big/\left[\beta_\infty^*\left(y_p\right)^2\right]$ and $\omega_{\log} = u_\tau\Big/\left(C_\mu^{1/2}\kappa y_p\right)$, where $\beta_\infty^* = 0.075$ .

## 3. Entropy transport equation

The total specific entropy of the mixture is computed by

$$s = s_{\text{in}}^* + \Delta s = s_{\text{in}}^* + \Delta s_v - \Delta s_l \tag{24}$$

where $\Delta s_v$ is entropy change of gas phase. The term $\Delta s_l$ is the entropy transfer into vapor phase during latent heat release.

In the transonic condensation flow, the specific entropy $s$ of wet steam is expressed as

$$s - s_{\text{in}}^* = s_{tran} + s_{gen} = s_{tran} + s_{gen,D} + s_{gen,C} + s_{gen,L} + s_{gen,A} \tag{25}$$

where $s_{tran}$ is the entropy transfer. The total entropy generation $s_{gen}$ includes four parts, namely, $s_{gen,D}$ , $s_{gen,C}$ , $s_{gen,L}$ and $s_{gen,A}$ which represent the entropy generations due to viscous, heat conduction, phase change and aerodynamic losses. The transport equation for entropy is a first order linear PDEs (partial differential equation) and satisfies the principle of superposition, because the velocity is independent on the entropy. Each part of entropy change is calculated by

$$\rho\frac{D\left(s_\phi\right)}{Dt}=\frac{\partial\rho s_\phi}{\partial t}+\frac{\partial}{\partial x_i}\left(\rho s_\phi\bar{u}_i\right)=Y_\phi \tag{26}$$

where the source terms are $Y_{tran}=\frac{\partial}{\partial x_i}\left(\frac{\lambda_{eff}}{T}\frac{\partial T}{\partial x_i}\right)$, $Y_{gen,D}=\frac{\bar{\Phi}}{T}$, $Y_{gen,C}=\frac{\overline{\Phi_\Theta}}{T}$, in which $Y_{gen,D}=Y_{gen,\bar{D}}+Y_{gen,D'}$ and $Y_{gen,C}=Y_{gen,\bar{C}}+Y_{gen,C'}$ considering the turbulence effect.

The viscous dissipation $Y_{gen,D}=\frac{\bar{\Phi}}{T}$ appears two groups of terms [34], one with mean and the other with fluctuating quantities, namely local viscous entropy generation rate, where $Y_{Gen,\bar{D}}$ is expressed by

$$Y_{Gen,\bar{D}}=\frac{2\mu S_{i,j}S_{i,j}}{T}=\frac{\mu}{\bar{\bar{T}}}\cdot\left[2\left\{\left(\frac{\partial\bar{u}}{\partial x}\right)^2+\left(\frac{\partial\bar{v}}{\partial y}\right)^2+\left(\frac{\partial\bar{w}}{\partial z}\right)^2\right\}+\left(\frac{\partial\bar{u}}{\partial y}+\frac{\partial\bar{v}}{\partial x}\right)^2+\left(\frac{\partial\bar{u}}{\partial z}+\frac{\partial\bar{w}}{\partial x}\right)^2+\left(\frac{\partial\bar{v}}{\partial z}+\frac{\partial\bar{w}}{\partial y}\right)^2\right] \tag{27}$$

where the mean strain rate $S_{i,j}$ is defined as $S_{i,j}=\frac{1}{2}\left(\frac{\partial\bar{u}_j}{\partial x_i}+\frac{\partial\bar{u}_i}{\partial x_j}\right)$. Following Wilcox model [35], the specific dissipation rate of turbulent kinetic energy $\omega$ is defined as $\omega=\varepsilon/\left(\beta^*k\right)$ with $\beta^*=C_\mu=0.09$ for SST $k$-$w$ model. Then, combining with the turbulent dissipation model [34], $Y_{Gen,D'}$ is calculated by

$$Y_{Gen,D'}=\frac{\rho\beta^*k\omega}{\bar{T}} \tag{28}$$

Entropy generation derived from heat conduction also contains two groups of terms, namely $Y_{gen,D}=\left(\overline{\Phi_\Theta/T^2}\right)=Y_{Gen,\bar{C}}+Y_{Gen,C'}$: The source term $S_{Gen,C}$ is

$$Y_{Gen,\bar{C}}=\frac{\lambda}{\bar{\bar{T}}^2}\left[\left(\frac{\partial\bar{T}}{\partial x}\right)^2+\left(\frac{\partial\bar{T}}{\partial y}\right)^2+\left(\frac{\partial\bar{T}}{\partial z}\right)^2\right] \tag{29}$$

According to turbulence model [34], the equation for the source term $S_{Gen,C'}$ therefore is

$$Y_{Gen,C'}=\frac{\alpha_t}{\alpha}Y_{Gen,C'}=\frac{\alpha_t}{\alpha}\frac{\lambda}{\overline{T}^2}\left[\left(\frac{\partial\overline{T}}{\partial x}\right)^2+\left(\frac{\partial\overline{T}}{\partial y}\right)^2+\left(\frac{\partial\overline{T}}{\partial z}\right)^2\right] \tag{30}$$

where, $\alpha$ is the thermal diffusivity of the fluid and equals $\lambda/\rho c_p$ . The turbulence thermal diffusivity $\alpha_t$ is expressed as $\alpha_t=\nu_t/Pr_t$ , where the value of $Pr_t$ is 0.85.

The entropy generation $S_{gen,L}$ during phase change of the condensation due to the temperature difference between liquid and vapor is simplified as [36]

$$Y_{gen,L}=\Gamma h_{lv}\left(\frac{1}{T_v}-\frac{1}{T_l}\right) \tag{31}$$

According to exergy rate balance equation for open system at steady state [37], the specific flow exergy $e_x$ is

$$e_x=h-h_0-T_0\left(s-s_0\right)+\frac{U^2}{2} \tag{32}$$

where the superscript ‘0’ denotes the system at the dead (environment) state.

The exergy destruction $e_D$ is equal to the entropy generation $s_{gen}$ within the system and temperature of reference environment $T_0$.

$$e_D=\Delta e_x=T_0 s_{gen} \tag{33}$$

The exergy destruction ratio $\zeta_D$ is defined as the ratio of irreversibility to net exergy of inlet fluid [20], thus

$$\zeta_D=\frac{e_D}{e_{x,\mathrm{in}}}=\frac{T_0\Delta s}{h_{\mathrm{in}}^*-h_0-T_0\left(s_{\mathrm{in}}^*-s_0\right)} \tag{34}$$

Besides, for better understanding the wetness loss, the performance loss coefficient of turbine blade cascade is also introduced and defined as follows [38],

$$\eta_{\text{Loss}} = 1 - \frac{h_{\text{in}} - h_{\text{out}}}{h_{\text{in}} - h_{out,dry}} = 1 - \frac{U_{out}^2}{U_{out,dry}^2} \tag{35}$$

in which the dry case denotes a dry expansion between inlet and outlet pressures the same as the wet expansion but changing inlet temperature to get the same outflow static temperature as the wet case.

## 4. Experimental validation

### *4.1. Numerical scheme*

The flowchart for simulation model is shown in Fig. 1. The two-dimensional computational domain is derived from Moore's nozzle B [39] and turbine blade cascade of Bakhtar et al. [40] for validating the present model. The structured quad-map meshes are adopted. The density-based solver with implicit formulation and Roe - FDS flux type is applied to the numerical calculation of governing equations for the two-phase flow. The second-order upwind scheme is employed to discretize the governing equations and the gradients are calculated using the least squares cell based gradient evaluation preserving a second-order spatial accuracy. The transition SST with different geometric roughness height is chosen as the viscous model. The total temperature and total pressure are set as inlet boundary conditions. The outlet static pressure is set as outlet condition.

For nozzle B, the inlet conditions are $p_{\text{in}}^* = 25$ kPa and $T_{\text{in}}^* = 357.6$ K. The corresponding saturated temperature $T_{sat,\text{in}} = 338.1$ K at stagnation condition. For the blade of Bakhtar, the inlet stagnation condition $p_{\text{in}}^*$ is equal to 172 kPa and $T_{\text{in}}^*$ is 380.66 K while the inlet saturation temperature $T_{sat,\text{in}}$ is 388.66 K. The outlet static pressure $p_{out}$ is $0.48p_{in}^*$. Besides, the turbulent intensity $Tu$ at inlet can be specified by

$$Tu = 0.16Re_{in}^{-1/8} \tag{36}$$

where the inlet Reynolds number $Re_{in}$ is equal to $3.05\times10^4$ in Bakhtar's experiment. Thus, the inlet turbulent intensity $Tu$ is 4.4% calculated by Eq. (36). Considering most researches used 5% as the medium turbulent intensity [41], the values of turbulent intensity $Tu$ in all cases are set to be 5% because we focus only on the effect of surface roughness in this study.

Fig. 1 The flowchart for simulation model.

*4.2. Validation results*

The geometry of nozzle B is shown in Fig. 2. There is a circular arc next to the throat and a line segment is tangent to it downstream. The structured mesh is refined near the throat and wall for better capturing the condensation process and viscous boundary layer. According to the grid-independent test, grid number in $x$ and $y$ directions is 450×110.

Fig. 2 The geometry and mesh of Nozzle B.

Fig. 3 The profiles of static pressure and droplet radius at the central line for Nozzle B.

Fig. 3 illustrates the static pressure ratio ($p/p_{in}^*$) profile and mean droplet size along the nozzle centerline obtained from present CFD and Moore's experiment. The dry flow denotes there is no condensation in the expansion process. The Wilson point calculated by the algebraic formula from Ref [42] is at $x$ = 78.4 mm, then a pressure jump occurs downstream resulted from the release of latent heat. In Fig. 3, the results of CFD are agree well with those of experiments. The presemt CFD model can accurately capture the position and intensity of condensing steam flow.

The geometry, mesh and boundary conditions of turbine blade of Bakhtar are given in Fig. 4. The length, chord and pitch sizes of the turbine blade are listed in Table 1, where the width of chamber data is specified for calculating the mass flow-rate, which is not reported in literature. The nominal throat of blade is about 4.914 mm. The inlet flow angle is 0°. The outlet angle of midline of passage $\varphi_{out}$ is 22.8°. The meshes of boundary layer were refined well to calculate the velocity distribution and wall shear stress accurately, which determine the value of entropy generation rate due to the viscous and heat conduction losses. According to the grid-independent test, the grid consists of 34,800 quadrilateral cells where the node number in $x$ and $y$ directions is 290×120.

Table 1 The geometry sizes for the turbine blade cascade.

Fig. 4 The geometry and mesh of turbine blade cascade by Bakhtar [40].

Fig. 5. Comparison of the static pressure distributions on the pressure and suction sides between numerical and experimental data in viscous wet case.

Fig. 5 shows the static pressure profiles on the pressure and suction sides of the smooth turbine blade. The CFD results coincide with the experimental data of Bakhtar. The position and intensity of condensation shock in the turbine blade can be predicted accurately by present CFD model. Besides, in order to ensure the prediction accuracy and reliability of entropy generation of viscous and heat conduction dissipations, the flow field of the boundary layer is assessed and validated.

The value of $Re_{throat}$ is equal to $1.135\times10^{5}$, thus boundary layer is laminar when blade surface is smooth and inlet turbulence intensity is medium. If the blade surface roughness or turbulent intensity is high enough, the transition from laminar to turbulent flow in boundary layer probably occurs in the rough blade. For quantitative validation, only dry case is utilized to evaluate the boundary layer.

The similarity solution of velocity profiles of laminar boundary layer over smooth wall of two-dimensional blade in dry case is computed as [43]

$$\frac{y}{d}=\frac{\left(\frac{\kappa+1}{2}\right)^{\frac{\kappa+3}{4(\kappa-1)}}}{\sqrt{R_{\mathrm{o}}\cdot m}}\left\{\sqrt{2}\mathrm{artanh}\sqrt{\frac{2+\frac{u}{u_1}}{3}}-\sqrt{2}\mathrm{artanh}\sqrt{\frac{2}{3}}+\frac{\kappa-1}{2}\left(\frac{2}{\sqrt{3}}-\sqrt{\frac{2}{3}}\left(1-\frac{u}{u_1}\right)\sqrt{\frac{u}{u_1}+2}\right)\right\} \quad (37)$$

where $u_1$ is the free stream velocity in the core region and $R_{\mathrm{o}}=\left[(\kappa+1)/2\right]^{\frac{\kappa+1}{2(\kappa-1)}}Re_{throat}$. The similar parameter is $m=\sqrt{d/R_c\left[(\kappa+1)/2\right]^{\frac{3\kappa-1}{\kappa-1}}}$ for two-dimensional blade nozzle.

In Fig. 6 (a), the results of velocity profiles of laminar boundary layer from CFD and similar solution in viscous dry case with smooth surface are plotted. The velocity magnitudes of the free stream around the suction side and pressure side are 495 m/s and 423 m/s. It indicates that the velocity profiles of CFD results are agree with similar solution. For the pressure side, the curve (similar solution) coincides exactly with the scatter (CFD).

Fig. 6 Comparison of velocity profiles of boundary layer between CFD, similar solution, empirical formula in viscous dry case.

If the wall boundary condition is changed from smooth to rough, the transition SST model can correlate the effect of surface roughness on the transition parameter and turbulent dissipation rate. The velocities of transition and turbulence boundary layer near rough wall of turbine blade are shown in Fig. 6 (b). When the roughness rises up to 50 μm, the boundary layer will be fully rough regime. Under this condition, the velocity profile of turbulent boundary layer meets the logarithmic law which coincides with the empirical formula. The results indicate transition SST model has good prediction accuracy for viscous boundary layer with surface roughness.

## 5. Flow field behaviors in smooth and rough blades

According to Eqs. (27)-(31), the various parts of entropy generation are dependent on flow field behaviors of condensing flow including the distributions and gradients of the velocity, temperature, condensation rate and the wetness of the wet flow. Thus, this complex flow field behaviors including wetness fraction, intermittency, turbulent viscosity, flow deviation angle and mass flux are discussed firstly.

### *5.1. Wetness fraction distribution*

Fig. 7 and Fig. 8 illustrate Mach number, subcooling and wetness fraction distributions in the turbine blade with different back pressure ratio $p_{out}/p_{in}^*$. The outflow is transonic for $p_{out}/p_{in}^*$ =0.48, while subsonic for $p_{out}/p_{in}^*$ = 0.72. In Fig. 7, a complex shock wave pattern occurs in the wake. The flow firstly generates an oblique shock over the pressure side at trailing edge and reflects at the suction side leading to a boundary layer separation and reattachment (shown in the next subsection). Then, the flow is accelerated and the velocity increases to supersonic again which is also observed by Kalitzin [44]. Thus, the wetness fraction firstly decreases through the oblique shock because an evaporation process will occur with the increase of vapor temperature (subcooling is less than 0), and then rises slightly due to secondary condensation with flow reacceleration and temperature drop.

Fig. 7 The distributions of Mach number, subcooling and wetness fraction for smooth blade cascade with $p_{out}/p_{in}^{*}$ =0.48.

It is shown in Fig. 8 that with the outflow pressure increasing to $p_{out}/p_{in}^{*}$ = 0.72, the outflow will be completely subsonic with the maximum Ma number of 0.85. The outlet wetness fraction decreases from 0.031 to 0.017 comparing with Fig. 7. Besides, the evaporation phenomenon also occurs during the pressure recovery process. Because the compression wave is relatively gentle during the pressure recovery and there is no secondary condensation at the outlet.

Fig. 8 The distributions of Mach number, subcooling and wetness fraction for smooth blade cascade with $p_{out}/p_{in}^{*}$ =0.72.

Fig. 9 The profiles of local wetness fraction at the outlet.

Fig. 9 presents the profiles of local wetness fraction at the outlet for five different back pressure and five different roughness values. It shows the outflow wetness fraction is not uniform, especially for the wake. In Fig. 9 (a), the wetness fraction $\beta$ gradually increases with the outlet back pressure decreasing which coincides with Fig. 7 and Fig. 8. Besides, the profile of wetness fraction has one valley near the wake in each condition. The value of valley will be larger with back pressure decreasing. As shown in Fig. 9 (a), the maximum drop of valley is about 0.0401 at $y$ = 0.651 mm for $p_{out}/p_{in}^*$ = 0.24. In Fig. 9 (b), it is found the roughness only affects the wetness fraction near the wake. This is because the wake is the region of disturbed flow depending on the boundary layer flow around the blade which is affected by the surface roughness. The maximum drop of valley is 0.00294 at $y$ = 12.081 mm for $K_s$ = 100 μm.

In conclusion, the dominant parameter of the local wetness fraction in free flow is back pressure, while both back pressure and surface roughness affect the local wetness fraction in wake region. Next, due to the wake flow is dependent on the boundary layer development around the blade, the intermittency of transition and turbulent properties should be investigated further.

### *5.2. Intermittency and turbulent viscosity*

The onset of transition is considered as the position of intermittency jump. The intermittency contour and streamline near the suction side and pressure side with $p_{out}/p_{in}^*$ = 0.48 in viscous dry and wet cases are plotted in Fig. 10. As shown in Fig. 10 (a)-(c), the transition onset locations over the pressure side are at $x$ = 34.95 mm (blade tail) in both viscous dry and wet cases with smooth surface, while the transition onset locations over the suction side are at $x$ = 30.68 mm and 32.00 mm in viscous dry case and wet case respectively. It means the vapor condensation results in the transition onset slightly moving towards the trail edge on the suction side due to the vapor condensation slows down the boundary layer development, but does not change the transition onset location on the pressure side. The transition onset location on the suction side is at $x$ = 31.30 mm in viscous wet case with roughness 10 m, as shown in Fig. 10 (d). When roughness increases up to 100 m, the transition onset location will continue to move upstream to reach leading edge ($x$ = 10.00 mm), as shown in Fig. 11.

Fig. 10 Intermittency contour and streamline of transition flow near the suction side and pressure side with $p_{out}/p_{in}^*$ = 0.48 in viscous dry and wet cases.

Fig. 11 presents the effects of roughness on the transition onset locations with $p_{out}/p_{in}^*$ = 0.48 in viscous dry and wet cases. The dominant parameter of transition onset location is the surface roughness. The coordinates of throat on pressure and suction sides are ($x$, $y$) = (32.75, 43.36) and (28.38, 41.13). The Wilson points on pressure and suction sides are $x$ = 32.46 and 27.87 mm. For the pressure side in viscous dry case, the transition onset will not move until the roughness reaches to 33 m. Then, the transition onset location will move upstream swiftly along with the increase of roughness. When the roughness is 33.16 m, the transition point reaches nominal throat ($x$ = 32.75 mm) and then moves to leading edge.

Fig. 11 The transition onset locations on the suction side and pressure side with $p_{out}/p_{in}^*$ = 0.48 in viscous dry and wet cases.

Fig. 12 The turbulent viscosity ratio contours in viscous wet cases.

The transition onset location determines whether or not the boundary layer is turbulent, and the turbulent viscosity changes accordingly. Fig. 12 presents the turbulent viscosity ratio contours in viscous wet case. The turbulent flow mainly occurs in the wake and boundary layer. For smooth blade with $p_{\mathrm{out}}/p_{\mathrm{in}}^* = 0.78$, the maximum turbulent viscosity ratio $\mu_t/\mu$ in the wake is about 44.6, while this value will slightly increase to 50.1 for $p_{\mathrm{out}}/p_{\mathrm{in}}^* = 0.48$. With roughness increasing to 100 μm, the maximum value of $\mu_t/\mu$ significantly increases up to 150. It means roughness plays a significant role in turbulent viscosity.

Fig. 13 The profiles of turbulent viscosity ratio at outlet with different roughness in viscous wet case.

Fig. 14 The profiles of local turbulent dissipation rate at the outlet with different back pressure ratio $p_{\mathrm{out}}/p_{\mathrm{in}}^*$ for smooth blade in viscous wet case.

The profiles of local turbulent viscosity ratio at the outlet with different roughness in viscous wet case are shown in Fig. 13. It can be seen that as the surface roughness increases, the turbulent viscosity ratio gradually increases. For smooth surface, the maximum $\mu_t/\mu$ at the outlet is 39.41 at $y$ = 11.21 mm. For roughness $K_s$ = 100 μm, the maximum $\mu_t/\mu$ at the outlet is 141.59 (increasing by 259%) at $y$ =13.53 mm. On the other hand, Fig. 14 shows the profiles of local turbulent dissipation rate at outlet with different back pressure $p_{\mathrm{out}}/p_{\mathrm{in}}^*$. The local turbulent dissipation rate increases with the outflow pressure reduction resulted from more rapid flow expansion. When back pressure ratio decreases from 0.72 to 0.24, the local maximum value of $\varepsilon$ increases from $2.34\times10^6$ at $y$ =12.01 mm to $4.27\times10^7$ at $y$ =2.521 mm.

Besides, all profiles in Fig. 9, Fig. 13 and Fig. 14 also illustrate the information of the wake locations at different conditions. It is known that the wake location is dependent on the deviation angle, thus, the deviation angle of wet steam also should be discussed.

*5.3. The deviation angle and mass flux*

According to the wake location in Fig. 13 and Fig. 14, the deviation angle $\varphi$ of the wet steam, defined in Fig. 12 , changes with the roughness $K_s$ and back pressure ratio $p_{out}/p_{in}^*$. The distributions of deviation angle $\varphi$ of the wet steam flow are illustrated by Schlieren picture and Mach number contour in Fig. 15. It shows that there is significant difference of two wakes between $p_{out}/p_{in}^*$ =0.36 and $p_{out}/p_{in}^*$ =0.72. As previously mentioned, an oblique shock wave at Ma = 1.40 is generated near the trailing edge for $p_{out}/p_{in}^*$ =0.36. The interaction between shock and boundary layer leads to the wake deflection and changes the deviation angle of wet steam flow.

Fig. 15 Schlieren picture and Mach number contour with different back pressure ratio $p_{out}/p_{in}^*$ in viscous wet flow around the smooth blade.

Fig. 16 presents the profiles of local deviation angle at the outlet in viscous wet flow. The outlet angle $\varphi_{out}$ of midline of passage is 22.8°. It indicates the deviation angle is also not uniform for different back pressure and surface roughness. In Fig. 16 (a), the profile of deviation angle $\varphi$ keeps at almost 17° when the back pressure ratio $p_{out}/p_{in}^*$ >0.48. Then, the deviation angle $\varphi$ apparently grows up to 33.16° with the back pressure decreasing from 0.48 to 0.24 because a stronger oblique shock wave occurs at the trailing edge in Fig. 15. The profiles of deviation angles for different roughness are variant where the maximum angle difference is about 3.1°, which is shown in Fig. 16 (b). However, in actual the mass flux is also uneven at the outlet, thus the mass-averaged deviation angle and wetness faction are more important for evaluating the wetness loss.

Fig. 16 The profiles of local deviation angle at the outlet in viscous wet flow.

Fig. 17 shows the profiles of local mass flux at the throat and outlet with different roughness $K_s$ for $p_{\mathrm{out}}/p_{\mathrm{in}}^* = 0.48$ in viscous wet flow. As shown in Fig. 17 (a), when roughness is 100 μm, the throat displacement thickness of boundary layer is larger than others. Its mass flow rate $Q_m$ is 0.1294 kg·s$^{-1}$ which is the lowest value in these cases which is due to the effect of surface roughness. In Fig. 17 (b), there is difference in local mass flux at the outlet among various roughness conditions. Combining with the results in Fig. 9 and Fig. 16, the mass-averaged wetness fraction and deviation angle are calculated accurately.

Fig. 17 The profiles of local mass flux at the throat and the outlet with different surface roughness $K_s$ in viscous wet flow.

The mass-average wetness fraction is defined as follows:

$$\beta_{avg} = \frac{\int \beta\rho\vec{U}\cdot d\vec{A}}{\int \rho\vec{U}\cdot d\vec{A}} = \frac{\sum \beta_i\rho_i\vec{U}_i\cdot d\vec{A}_i}{\sum \rho_i\vec{U}_i\cdot d\vec{A}_i} \tag{38}$$

where $U$ and $A$ represent local velocity and the area. Table 2 shows all results of the mass-average wetness fraction $\beta_{avg}$ at the outlet with different roughness and back pressure. It indicates the mass-averaged wetness fraction decreases with the increase of $p_{\mathrm{out}}/p_{\mathrm{in}}^*$ and roughness. The roughness effect on mass-averaged wetness fraction $\beta_{avg}$ at the outlet is quite smaller than the effect of back pressure. For the smooth blade, the range of $\beta_{avg}$ is from 0.01669 to 0.05681.

Besides, the mass-averaged deviation angles $\varphi_{avg}$ at the outlet with different conditions are also obtained, as listed in Table 3. It is also indicated that the dominant parameter of mass-averaged deviation angle is back pressure ratio. But it should be noticed the surface roughness is the dominant parameter of viscous and thermodynamic losses which has been discussed in subsection 5.2.

Table 2 The mass-averaged wetness fraction $\beta_{avg}$ at the outlet with different roughness $K_s$ and back pressure ratio $p_{\mathrm{out}}/p_{\mathrm{in}}^*$.

Table 3 The mass-averaged deviation angle $\varphi_{avg}$ at the outlet with different roughness $K_s$ and back pressure ratio $p_{\mathrm{out}}/p_{\mathrm{in}}^*$.

## 6. Exergy destruction

According to the above analysis, each part of entropy generation due to viscous loss, heat conduction loss, phase change and aerodynamic loss of compressible fluid were calculated and analyzed. Then, the performance loss coefficient was obtained and discussed in detail.

### *6.1. Entropy generation*

In $p_{\mathrm{out}}/p_{\mathrm{in}}^*$ =0.36, the entropy generation $s_{gen,L}$, $s_{gen,D}$, $s_{gen,C}$ and $s_{gen,A}$ caused by the phase change, viscous, heat conduction and aerodynamic loss in wet flow around the smooth blade are plotted in Fig. 18. The entropy generation $s_{gen,L}$ is mainly distributed in vapor condensation and evaporation regions. $s_{gen,D}$, which is the sum of the mean and fluctuating quantities of viscous loss, is mainly distributed in boundary layer, wake and condensation shock regions. $s_{gen,C}$ is generated at the boundary layer and wake regions. The $s_{gen,A}$ caused by aerodynamic loss is located at the whole domain, due to the multi-dimensional non-isentropic characteristic and liquid-vapor mass transfer which still exists in the inviscid flow. The local maximum value of four parts of entropy generation are about 13.5, 39.8, 80.5 and 68.7 J·kg$^{-1}$·K$^{-1}$.

Fig. 18 The contours of various parts of entropy generation in viscous wet flow around the smooth blade with $p_{\mathrm{out}}/p_{\mathrm{in}}^{*}$ =0.36

Table 4 Each part of mass-averaged entropy generation (J·kg$^{-1}$·K$^{-1}$) at the outlet in viscous wet flow ($p_{\mathrm{out}}/p_{\mathrm{in}}^{*}$ = 0.36) with different roughness $K_s$.

Table 4 presents the mass-averaged entropy generation at the outlet in viscous wet flow for $p_{\mathrm{out}}/p_{\mathrm{in}}^{*}$ =0.36 with different roughness. The roughness effect on $s_{gen,D'}$ due to turbulent viscous loss increases by 478%, $s_{gen,\bar{C}}$ due to the mean temperature gradient increases by 180%, $s_{gen,C'}$ due to turbulent heat conduction loss increases by 3195%. Besides, the roughness also affects the multi-dimensional and non-isentropic characteristic which will slightly change the value of $s_{gen,A}$ from 33.002 to 37.392 J·kg$^{-1}$·K$^{-1}$. For better understanding the aerodynamic loss, the comparison of entropy generation between inviscid dry, viscous dry and viscous wet flows are shown in Table

5.

In inviscid dry case when the back pressure ratio $p_{out}/p_{in}^*$ decreases from 0.72 to 0.24, the value of $s_{gen,A}$ increases from 0.389 to 19.008 J·kg$^{-1}$·K$^{-1}$. This means the greater the velocity gradient is, the more $s_{gen,A}$ is generated by aerodynamic loss. Compared with inviscid dry, the value of $s_{gen,A}$ will slightly decrease due to the viscous force will dissipate the propagation and reflection of compression and expansion waves, but the total entropy generation is larger than those in inviscid dry case. Then, compared with viscous dry and wet case, it is revealed that the condensation and evaporation processes form the new entropy generation $s_{gen,L}$ and increase the value of $s_{gen,A}$ due to the local density change during the liquid-vapor mass transfer. The total entropy generation in smooth blade increases from 19.008 J·kg$^{-1}$·K$^{-1}$ in inviscid dry case to 66.185 J·kg$^{-1}$·K$^{-}$1 in viscous wet case when $p_{out}/p_{in}^*$ =0.24.

Table 5 The mass-averaged entropy generations (J·kg$^{-1}$·K$^{-1}$) at the outlet in inviscid dry, viscous dry, viscous wet flows around the smooth blade with back pressure ratio $p_{out}/p_{in}^*$.

Fig. 19 shows the stacked column of entropy generation at the outlet in viscous wet flow with respect to roughens and back pressure ratio. Table 6 presents the corresponding values of total entropy generation. With back pressure ratio increasing, the flow slows down and the momentum and thermodynamic irreversibility decrease resulting in a lower entropy generation. $s_{gen,A}$ and $s_{gen,L}$ is mainly affected by back pressure ratio. The reason is that the wetness fraction is correlated with back pressure ratio as shown in Table 2. Besides, the dominant parameter of $s_{gen,D}$ and $s_{gen,C}$ is surface roughness. The maximum value of total entropy generation is 84.520 J·kg$^{-1}$·K$^{-1}$ when $K_s$ = 100 μm and $p_{out}/p_{in}^*$ = 0.24, while the minimum value is 26.248 when $K_s$ = 0 μm and $p_{out}/p_{in}^*$ = 0.72 in these cases.

Fig. 19 The stacked column of mass-averaged entropy generations at the outlet in viscous wet flow with different roughness $K_s$ and back pressure ratio $p_{out}/p_{in}^*$.

Table 6 The total entropy generation (J·kg$^{-1}$·K$^{-1}$) at the outlet in viscous wet flow with different roughness $K_s$ and back pressure ratio $p_{out}/p_{in}^*$.

Fig. 20 presents the percentages of each part of entropy generation in viscous wet flow. For example, when $p_{out}/p_{in}^*$ =0.24, $s_{gen,D}$ increases from 21.38% to 27.43%, and $s_{gen,C}$ grows from 1.19% to 6.77% when the roughness is 100 μm. When $p_{out}/p_{in}^*$ =0.72, $s_{gen,D}$ grows from 15.10% to 27.43%, and $s_{gen,D}$ grows from 0.89% to 4.29%. These changes mainly attribute to the surface roughness.

Fig. 20 The percentages of each part of mass-averaged entropy generation at the outlet in viscous wet flow with different conditions.

### *6.2. Exergy destruction ratio*

The results of the performance loss coefficient $\eta_{\mathrm{Loss}}$ calculated by Eq. (35) are shown in Fig. 21. For $p_{out}/p_{in}^*$ = 0.72 and wetness fraction $\beta_{avg}$ = 0.01495 ~ 0.01669 in

Table 2, the performance loss coefficient $\eta_{\text{Loss}}$ = 0.0324 ~ 0.0961. For $p_{\text{out}}/p_{\text{in}}^*$ = 0.24 and $\beta_{avg}$ = 0.0541 ~ 0.0568, $\eta_{\text{Loss}}$ = 0.0856 ~ 0.1171. A classical Baumann rule [45] for wetness loss of the steam turbine where the wet total efficiency against the dry efficiency is $\eta_{\text{Loss}} = (1 - a_{wet}\beta)$, where $a_{wet}$ is Baumann factor. In this study, $a_{wet}$ =1.34 and 1.29 for $p_{\text{out}}/p_{\text{in}}^*$ = 0.48 and 0.60 in smooth blade.

Fig. 21 The performance loss coefficient at the outlet in viscous wet flow with different roughness $K_s$ and back pressure ratio $p_{\text{out}}/p_{\text{in}}^*$.

In present study, the inlet stagnation condition $p_{\text{in}}^*$ and $T_{\text{in}}^*$ are constant, namely $p_{\text{in}}^* \equiv 172$ kPa and $T_{\text{in}}^* \equiv 380.66$ K. The environment condition is set to be the same value as the steam condenser. Thus, the environment temperature $T_0$ is 298 K and pressure $p_0$ is 3.14 kPa at saturation state where the system has the maximum useful work possible [46]. Thus $s_{\text{in}}^*$-$s_0$ = -1.38 kJ·kg$^{-1}$. The inlet specific flow exergy $e_{x,\text{in}}$ = 568.4 kJ·kg$^{-1}$. The calculating values of the exergy destruction ratio $\zeta_D$ according to the Eq. (34) are listed in Table 7, in which exergy destruction ratio $\zeta_D$ grows with roughness increasing or back pressure decreasing. The maximum exergy destruction is 25.187 kJ/kg and the corresponding outlet $\beta_{avg}$ = 0.054 and exergy destruction ratio $\zeta_D$ = 4.43% when $p_{\text{out}}/p_{\text{in}}^*$ = 0.24 and $K_s$ = 100 μm. The value of exergy destruction ratio $\zeta_D$ is equal to (0.61~0.82) $\beta_{avg}$ for smooth blade, while the result is (0.81~1.17) $\beta_{avg}$ for $K_s$ = 100 μm.

Table 7 The exergy destruction ratio $\zeta_D$ at the outlet with different roughness $K_s$ and back pressure ratio $p_{\text{out}}/p_{\text{in}}^*$.

## 7. Conclusion

The entropy generation and exergy destruction of condensing steam flow for turbine blade with roughness were investigated. The compressible RANS equations including entropy transport equation with condensation model, transition SST model and roughness correlation were built. A good agreement between numerical and experimental results of static pressure and velocity boundary layer was achieved. Then, the flow field behaviors of wet steam and exergy destruction ratio were analyzed. The conclusions are as follows:

(1) The dominant parameter of local wetness fraction $\beta$ is $p_{\mathrm{out}}/p_{\mathrm{in}}^*$ in free stream, while roughness $K_s$ is also a crucial parameter in wake region. The mass-averaged $\beta_{avg}$ at outlet decreases with the increase of $p_{\mathrm{out}}/p_{\mathrm{in}}^*$ and roughness. However, the roughness effect on $\beta_{avg}$ is quite smaller than that of $p_{\mathrm{out}}/p_{\mathrm{in}}^*$. The range of $\beta_{avg}$ is from 0.01669 to 0.05681 in smooth blade.

(2) Roughness plays a significant role in the intermittency and turbulent viscosity. For roughness $K_s$ = 100 μm, the maximum $\mu_t/\mu$ at the outlet is 141.59 increasing by 259%.

(3) The dominant parameter of mass-averaged deviation angle $\varphi_{avg}$ is $p_{\mathrm{out}}/p_{\mathrm{in}}^*$. The range of $\varphi_{avg}$ is 16.974°~25.642° where outlet angle of passage midline $\varphi_{\mathrm{out}}$ is 22.8°. The roughness $K_s$ only changes the local value of deviation angle, namely distribution characteristic.

(4) For $p_{\mathrm{out}}/p_{\mathrm{in}}^*$ =0.24 in wet case, the roughness effect on $s_{gen,D'}$ increases by 478% and $s_{gen,C'}$ increases by 3195%. Besides, the roughness also slightly

changes $s_{gen,A}$ from 33.002 to 37.392 J·kg$^{-1}$·K$^{-1}$.

(5) The total entropy generation and exergy destruction increase with the increase of $K_s$ or the decrease of $p_{out}/p_{in}^*$. The maximum value of total entropy generation is 84.520 J·kg$^{-1}$·K$^{-1}$. For $p_{out}/p_{in}^*$ = 0.24 and $\beta_{avg}$ = 0.0541 ~ 0.0568, $\eta_{Loss}$ = 0.0856 ~ 0.1171. Besides, Baumann factor $a_{wet}$ =1.34 for $p_{out}/p_{in}^*$ = 0.48 in smooth blade.

(6) The maximum exergy destruction is 25.187 kJ·kg$^{-1}$, the corresponding outlet $\beta_{avg}$ = 0.054 and exergy destruction ratio is 4.43% when $p_{out}/p_{in}^*$ = 0.24 and $K_s$ = 100 μm.

This study provides an insight into entropy generation and exergy efficiency in turbine blade considering the influences of roughness and back pressure ratio. It may be utilized to evaluate possible improvement of the turbine system and guide the shape optimization.

## Acknowledgement

This work is supported by National Natural Science Foundation of China under Grant 51876143, 61873184, and 61627803, Natural Science Foundation of Tianjin under Grant 16JCQNJC03700 and 18JCQNJC74500.

## References

[1]. Dykas S, Majkut M, Smolka K, et al. Study of the wet steam flow in the blade tip rotor linear blade cascade. Int J Heat Mass Transf 2018;120:9-17.

[2]. Joseph J, Subramanian S, Vigney K, et al. Thermodynamic wetness loss calculation in nozzle and turbine cascade: nucleating steam flow. Heat Mass Transf 2018;54:2521-2531.

[3]. Zhang G, Wang L, Zhang S, et al. Effect evaluation of a novel dehumidification structure based on the modified model. Energy Convers Manage 2018;159:65-75.
[4]. Keisari JS, Shams M. Shape optimization of nucleating wet-steam flow nozzle. Appl Therm Eng 2016;103:812-820.
[5]. Voldsund M, Nguyen T, Elmegaard B, et al. Exergy destruction and losses on four North Sea offshore platforms: A comparative study of the oil and gas processing plants. Energy 2014;74:45-58.
[6]. Bellucci J, Rubechini F, Marconcini M, et al. The influence of roughness on a high-pressure steam turbine stage: an experimental and numerical study. J Eng Gas Turbines Power, 2014;137:1-9.
[7]. Young JB, Two-dimensional, nonequilibrium, wet-steam calculations for nozzles and turbine cascades. J Turbomach 1992;114:569-579.
[8]. Bakhtar F, Zamri MY, Rodriguez-Lelis JM. A comparative study of treatment of two-dimensional two-phase flows of steam by a Runge-Kutta and by Denton’s methods. J. Mechanical Engineering Science, 2007;221:689-706.
[9]. Shehata AS, Saqr KM, Xiao M, et al. Performance analysis of wells turbine blades using the entropy generation minimization method. Renew Energ 2016;86:1123-1133.
[10]. Li D, Wang H, Qin Y, et al. Entropy production analysis of hysteresis characteristic of a pump-turbine model. Energ Convers Manage 2017; 149:175-191.
[11]. Haseli Y. Efficiency improvement of thermal power plants through specific entropy generation. Energ Convers Manage 2018;159:109-120.
[12]. Peña-Lamas J, Martinez-Gomez J, Martín M, et al. Optimal production of power from mid-temperature geothermal sources: Scale and safety issues. Energ Convers

Manage 2018;165:172-182.
[13]. Ghisu T, Cambuli F, Puddu P, et al. Numerical evaluation of entropy generation in isolated airfoils and Wells turbines. Meccanica 2018;53:3437-3456.
[14]. Rajabi V, Amani E. A computational study of swirl number effects on entropy generation in gas turbine combustors. Heat Transfer Eng 2019;40(3-4):346-361.
[15]. Dykas S, Majkut M, Strozik M, et al. Losses estimation in transonic wet steam flow through linear blade cascade. J Therm Sci 2015;24(2):109-116.
[16]. Bagheri-Esfe H, Kermani MJ, Saffar-Avval M. Effects of non-equilibrium condensation on aerodynamics of the flow field in a steam turbine cascade. Sci Iran 2017;24(2):624-636.
[17]. Vatanmakan M, Lakzian E, Mahpeykar MR. Investigating the entropy generation in condensing steam flow in turbine blades with volumetric heating. Energy 2018;147:701-714.
[18]. Kaska. O. Energy and exergy analysis of an organic Rankine for power generation from waste heat recovery in steel industry. Energy Convers Manage 2014;77:108-117.
[19]. Şöhret Y, Ekici S, Altuntaş Ö, et al. Exergy as a useful tool for the performance assessment of aircraft gas turbine engines: A key review. Prog Aerosp Sci 2016;83:57-69.
[20]. Vučković GD, Stojiljković MM, Vukić, MV. First and second level of exergy destruction splitting in advanced exergy analysis for an existing boiler. Energy Convers Manage 2015;104:8-16.
[21]. Zhao Y, Wang S, Ge M, et al. Energy and exergy analysis of thermoelectric generator system with humidified flue gas. Energy Convers Manage

2018;156:140-149.

[22]. Chen W, Li Z, Sun Q, et al. Energy and exergy analysis of proposed compression-absorption refrigeration assisted by a heat-driven turbine at low evaporating temperature. Energy Convers Manage 2019;191:55-70.

[23]. Kind RJ, Serjak PJ, Abbott MWP. Measurements and prediction of the effects of surface roughness on profile losses and deviation in a turbine cascade. J Turbomach 1996;120(1):20-27.

[24]. Boyle RJ, Senyitko RG. Measurements and predictions of surface roughness effects on turbine vane aerodynamics. ASME Turbo Expo, Int. Joint Power Generation Conf, American Society Mech Eng 2003.

[25]. Bai T, Liu J, Zhang W. Effect of surface roughness on the aerodynamic performance of turbine blade cascade. J. Propul. Power, 2014;3(2):82-89.

[26]. Zhang Q, Goodro M, Ligrani PM, et al. Influence of surface roughness on the aerodynamics losses of a turbine vane. J Fluid Eng 2006;128(3):568-578.

[27]. Montomoli F, Hodson H, Haselbach F. Effect of roughness and unsteadiness on the performance of a new low pressure turbine blade at low Reynolds numbers. J Turbomach 2010;132:0310181-89.

[28]. Vazquez R, Torre D. The effect of surface roughness on efficiency of low pressure turbines. J Turbomach 2014;136(6):061008.

[29]. Kellersmann A, Weiler S, Bode C, et al. Surface roughness impact on low-pressure turbine performance due to operational deterioration. J Eng Gas Turb Power 2018;140:062601-1-062601-7.

[30]. Estemad S, Behrang A, Mohammadmoradi P, et al. Effects of surface roughness and mineral heterogeneity on pore-scale steam condensation. J Petrol Sci Eng

2017;159:624-634.
[31]. Esfe HB, Kermani MJ, Avval MS. Effects of surface roughness on deviation angle and performance losses in wet steam turbines. Appl Therm Eng 2015;90:158-173.
[32]. Bakhtar F, Young JB, White AJ, et al. Classical nucleation theory and its application to condensing steam flow calculations. J Mech Eng Sci 2005;219(12):1315–1333.
[33]. Stripf M, Schulz A, Bauer HJ, et al. Extended models for transitional rough wall boundary layers with heat transfer-Part I: model formulations. J Turbomach 2009;131(3): 031016.
[34]. Kock F, Herwig H. Entropy production calculation for turbulent shear flows and their implementation in CFD codes. Int J Heat Fluid Flow 2005;26(4): 672-680.
[35]. Bredberg J. On two-equation eddy-viscosity models. Department of Thermo and Fluid Dynamics, Chalmers University of Technology, Göteborg, Sweden, 2001.
[36]. Kermani MJ, Gerber AG. A general formula for the evaluation of thermodynamic and aerodynamic losses in nucleating steam flow. Int J Heat Mass Transf 2003;46:3265-3278.
[37]. Moran MJ, Shapiro HN, Boettner D, et al. Fundamentals of engineering thermodynamics. John Wiley and Sons, 2010, Dec 7.
[38]. Abadi SMANR, Ahmadpour A, Abadi SMNR, et al. CFD-based shape optimization of steam turbine blade cascade in transonic two phase flows. Appl Therm Eng 2017;112:1575-1589.
[39]. Moore MJ, Walters PT, Crane RI, et al. Predicting the fog drop size in wet steamturbines, in: Wet Steam 4 Conference, Institute of Mechanical Engineers (UK), University of Warwick, 1973:37-73.

[40]. Bakhtar F, Mahpeykar MR, Abbas K. An investigation of nucleating flows of steam in a cascade of turbine blading-theoretical treatment. J Fluid Eng 1995;117(1): 138-144.

[41]. Nazeryan M, Lakzian E. Detailed entropy generation analysis of a Wells turbine using the variation of the blade thickness. Energy 2018;143:385-405.

[42]. Ding H, Wang C, Wang G. Analytic equations for the Wilson point in high pressure steam flow through a nozzle. Int J Heat Mass Transf 2015;91:961–968.

[43]. Wang C, Wang X, Ding H. Boundary layer of non-equilibrium condensing steam flow in a supersonic nozzle. Appl Therm Eng 2018;129:389-402.

[44]. Kalitzin G, Iaccarino G. Computation of heat transfer in a linear turbine cascade. Center Turbulence Res Annu Res Briefs 1999: 277-288.

[45]. Baumann K. Some recent developments in large steam turbine practice. J Inst Electr Eng 1921;59:565–623.

[46]. Beer JM. High efficiency electric power generation: The environmental role. Prog Energ Combust 2007;33:107-134.

**List of Figure Captions and Table Titles**

pressure ratio *pout*/*pin** for smooth blade in viscous wet case.

Fig. 15 Schlieren picture and Mach number contour with different back pressure ratio *pout*/*pin** in viscous wet flow around the smooth blade.

Fig. 16 The profiles of local deviation angle at the outlet in viscous wet flow.

Fig. 17 The profiles of local mass flux at the throat and the outlet with different surface roughness *Ks* in viscous wet flow.

Fig. 18 The contours of various parts of entropy generation in viscous wet flow around the smooth blade with *pout*/*pin** =0.36

Fig. 19 The stacked column of mass-averaged entropy generations at the outlet in viscous wet flow with different roughness *Ks* and back pressure ratio *pout*/*pin**.

Fig. 20 The percentages of each part of mass-averaged entropy generation at the outlet in viscous wet flow with different conditions.

Fig. 21 The performance loss coefficient at the outlet in viscous wet flow with different roughness *Ks* and back pressure ratio *pout*/*pin**.

Table 1 The geometry sizes for the turbine blade cascade.

Table 2 The mass-averaged wetness fraction *βavg* at the outlet with different roughness *Ks* and back pressure ratio *pout*/*pin**.

Table 3 The mass-averaged deviation angle *φ*avg at the outlet with different roughness *Ks* and back pressure ratio *pout*/*pin**.

Table 4 Each part of mass-averaged entropy generation (J·kg-1·K-1) at the outlet in viscous wet flow (*pout*/*pin** = 0.36) with different roughness *Ks*.

Table 5 The mass-averaged entropy generations (J·kg-1·K-1) at the outlet in inviscid dry, viscous dry, viscous wet flows around the smooth blade with back pressure ratio *pout*/*pin**.

Table 6 The total entropy generation (J·kg-1·K-1) at the outlet in viscous wet flow with different roughness *Ks* and back pressure ratio *pout*/*pin**.

Table 7 The exergy destruction ratio $\zeta_D$ at the outlet with different roughness *Ks* and back pressure ratio *pout*/*pin**.

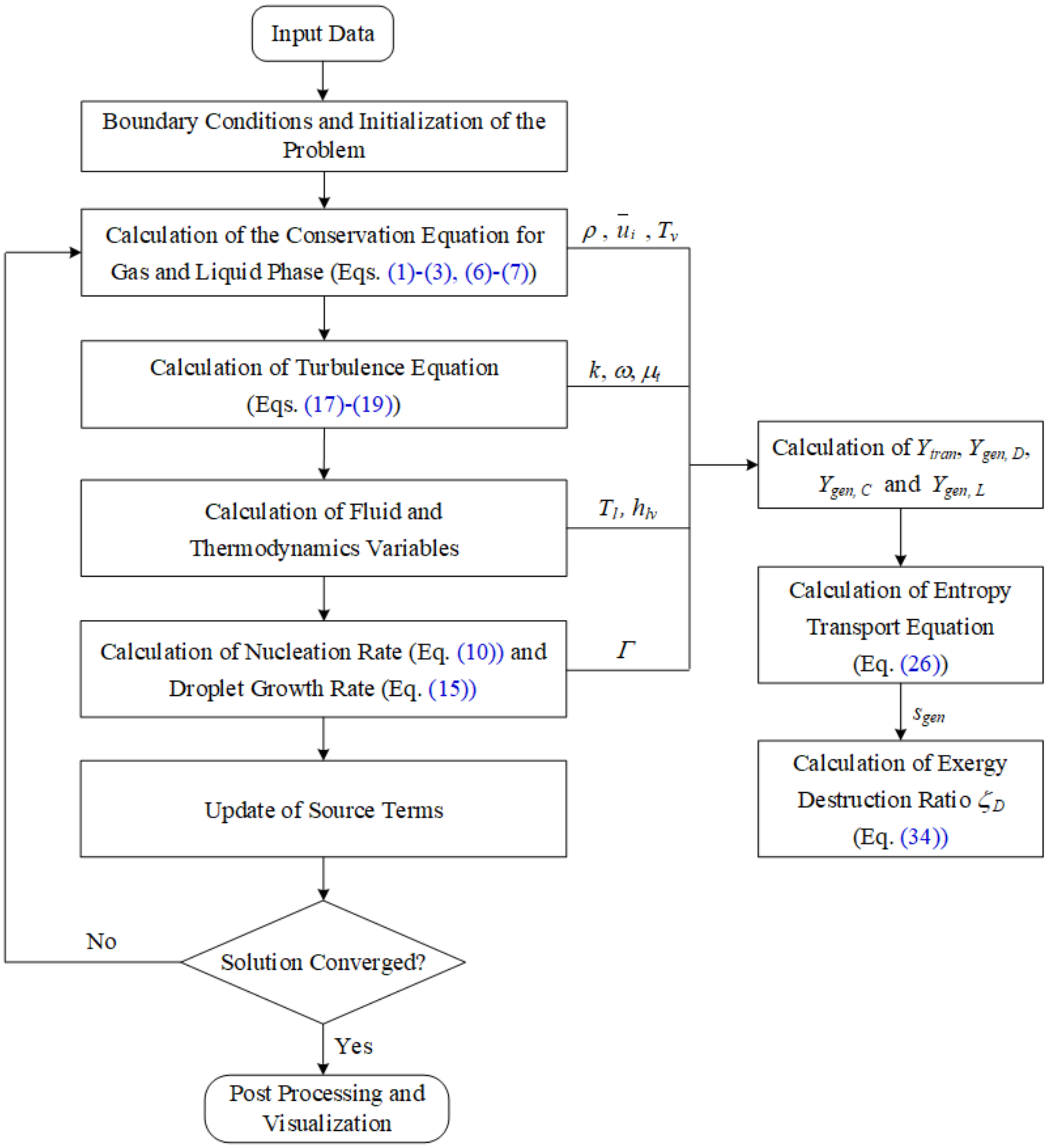

Fig. 22 The flowchart for simulation model.

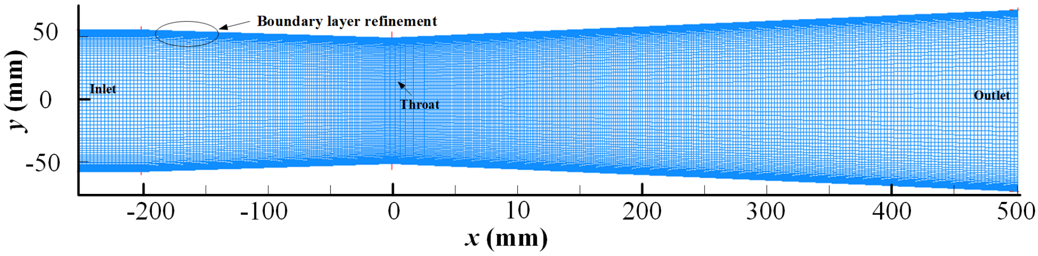


Fig. 23 The geometry and mesh of Nozzle B.

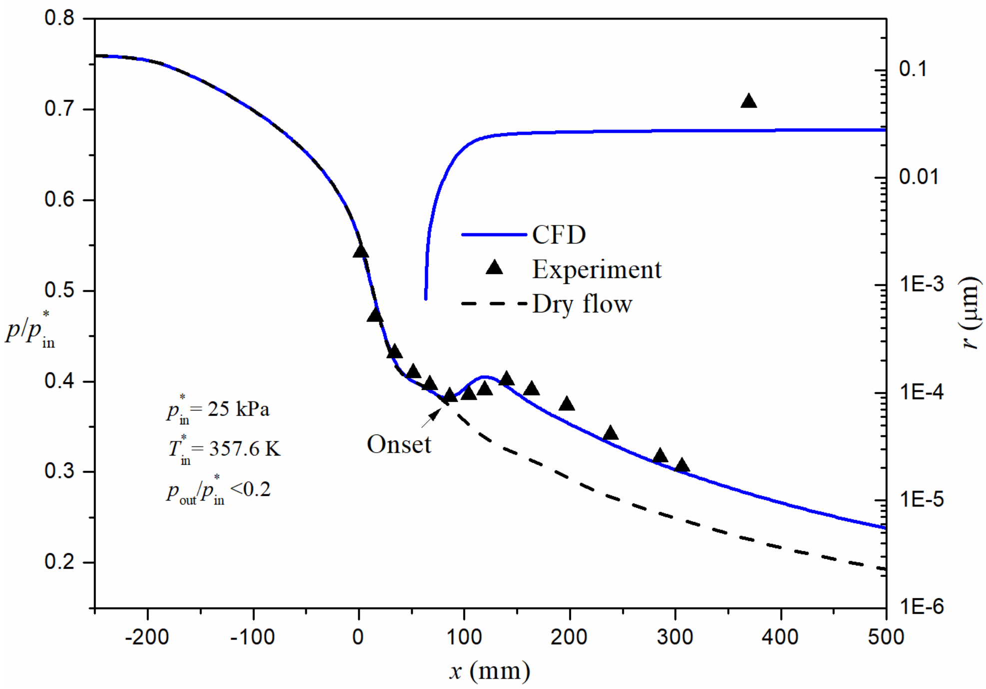

Fig. 24 The profiles of static pressure and droplet radius at the central line for Nozzle B.

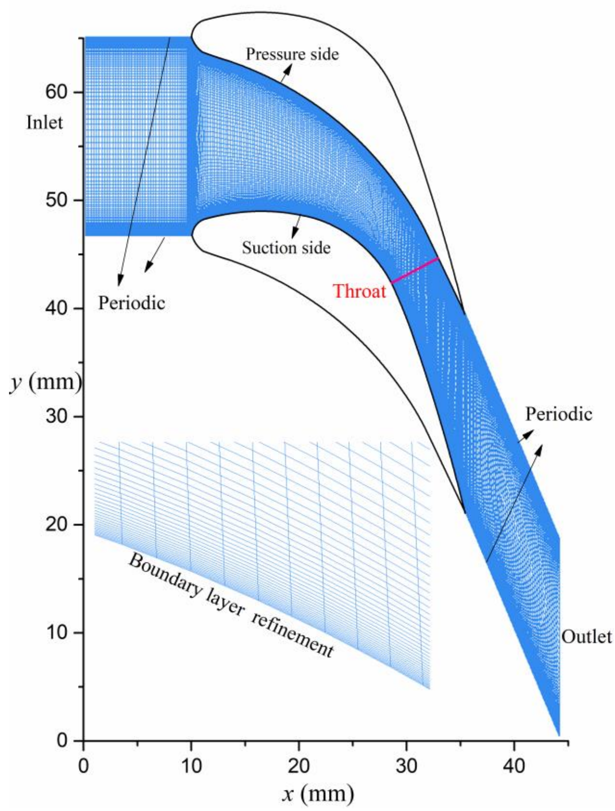

Fig. 25 The geometry and mesh of turbine blade cascade by Bakhtar [40].

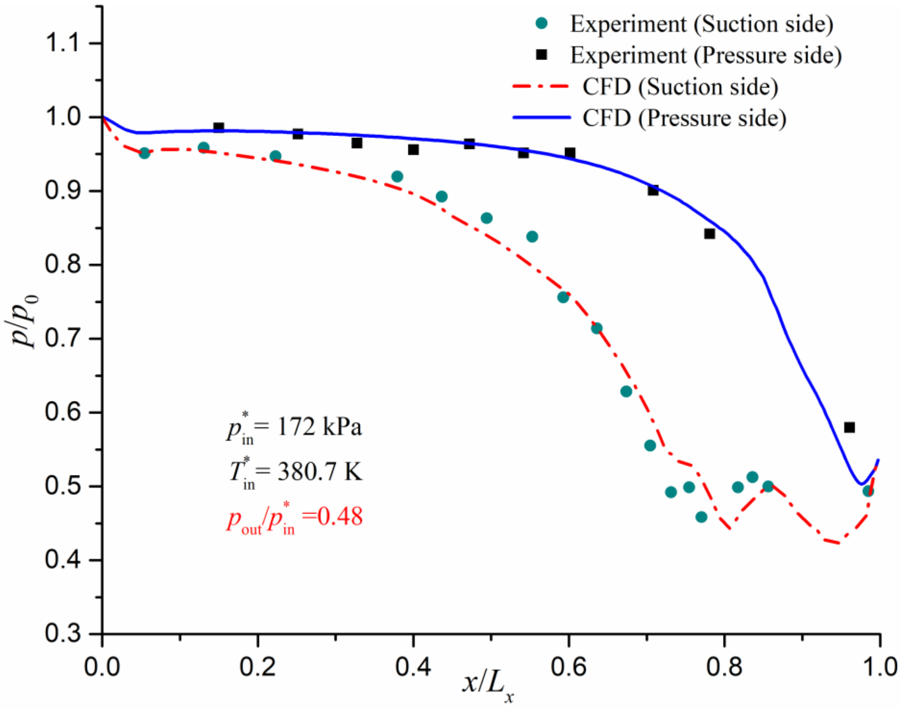


Fig. 26. Comparison of the static pressure distributions on the pressure and suction sides between numerical and experimental data in viscous wet case.

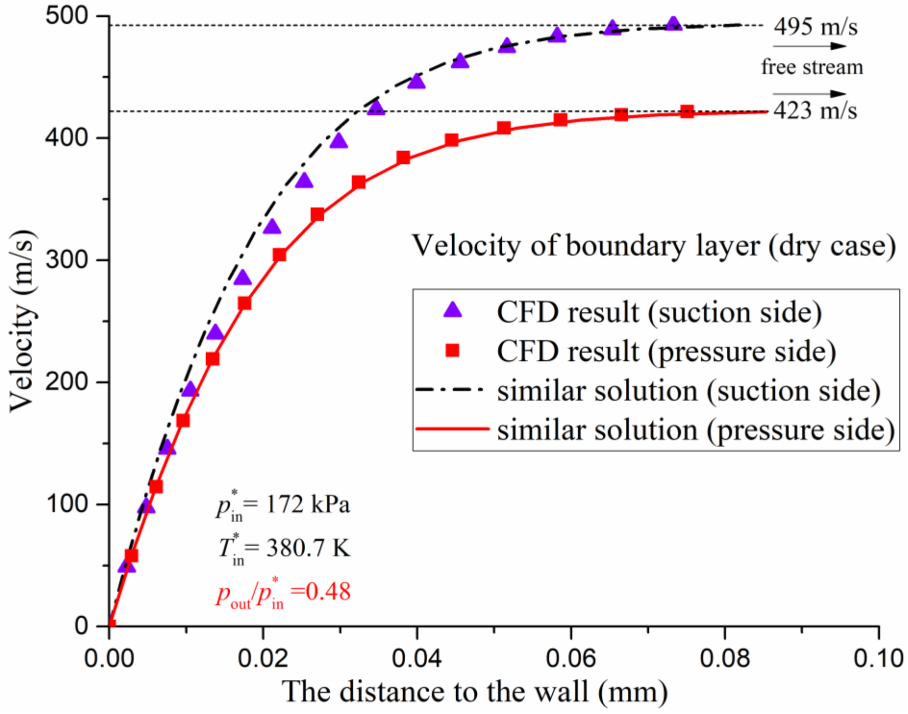


(a) Laminar boundary layer near the smooth wall

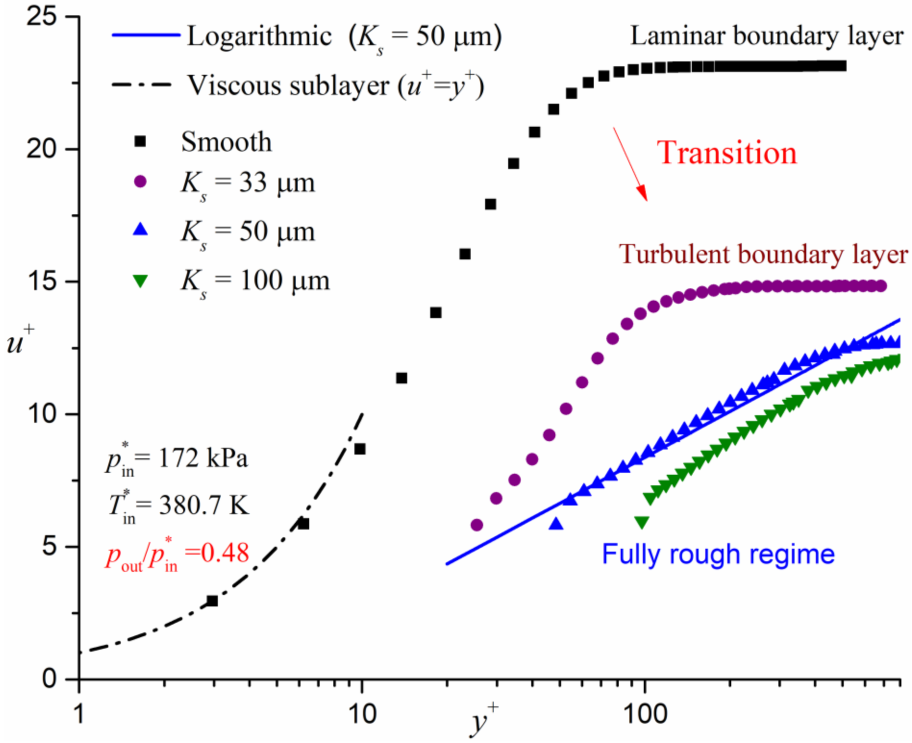


(b) Transition and turbulent boundary layer over rough wall

Fig. 27 Comparison of velocity profiles of boundary layer between CFD, similar solution, empirical formula in viscous dry case.

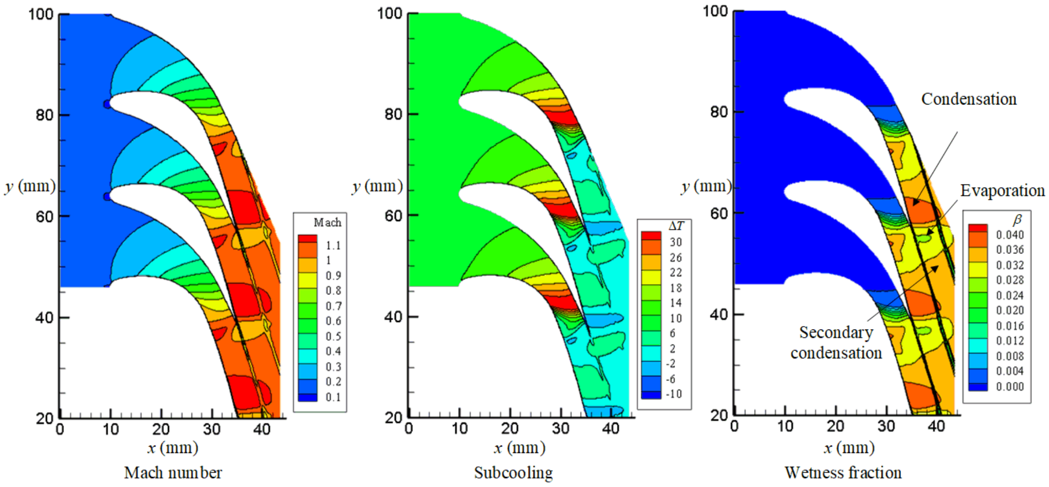


Fig. 28 The distributions of Mach number, subcooling and wetness fraction for smooth blade cascade with $p_{out}/p_{in}^{*}$ =0.48.

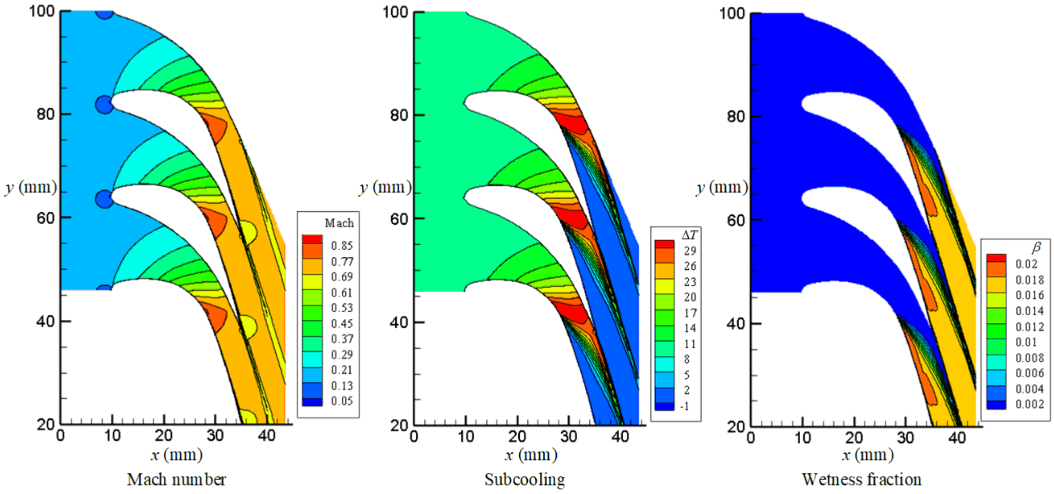


Fig. 29 The distributions of Mach number, subcooling and wetness fraction for smooth blade cascade with $p_{out}/p_{in}^{*}$ =0.72.

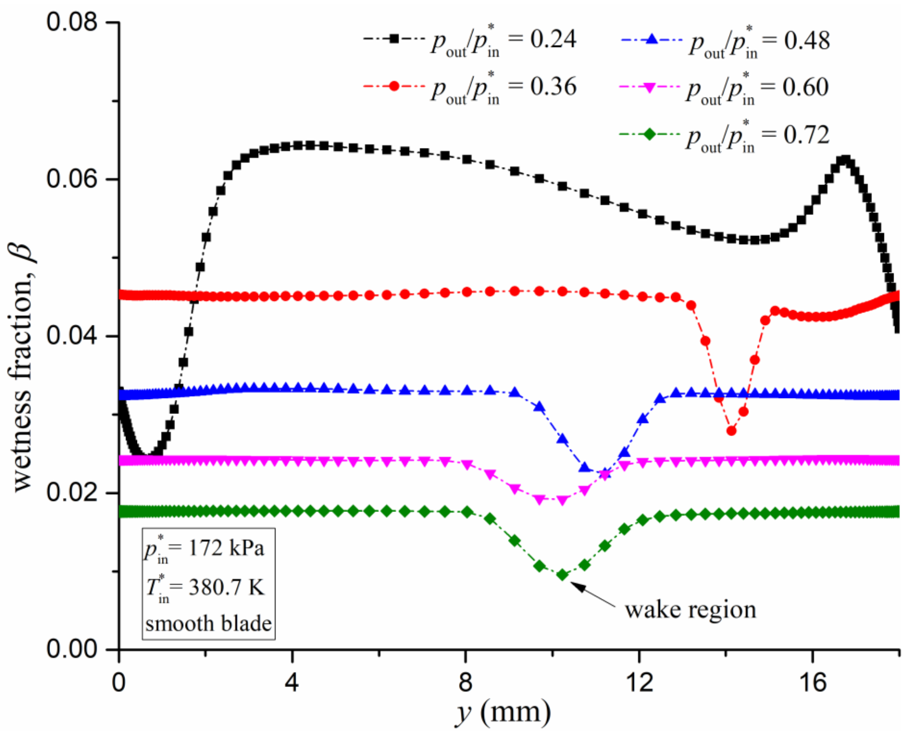


(a) different back pressure ratio $p_{out}/p_{in}^*$

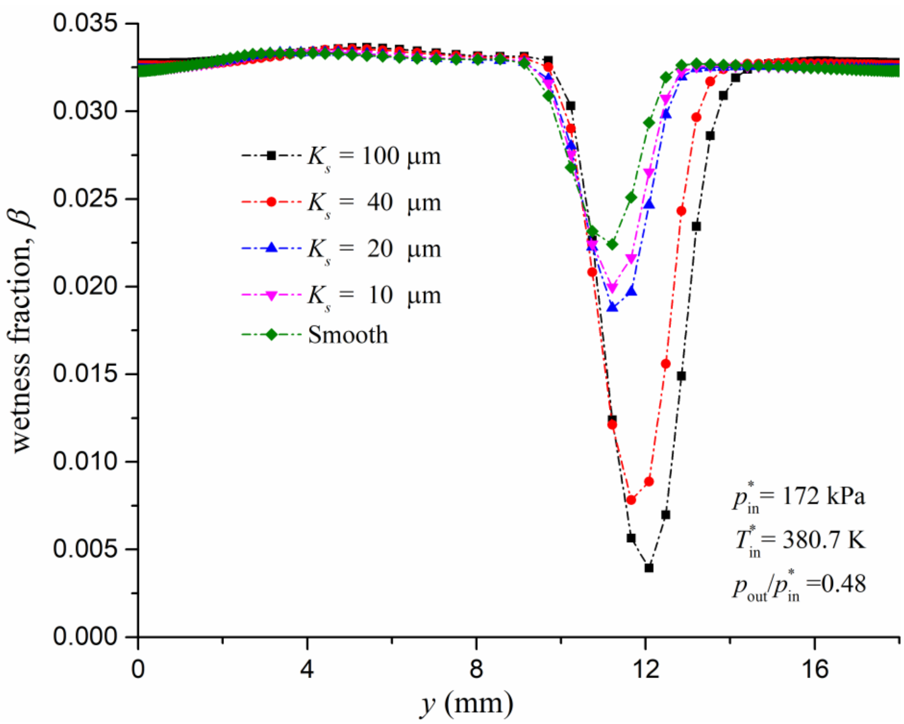


(b) different roughness $K_s$

Fig. 30 The profiles of local wetness fraction at the outlet.

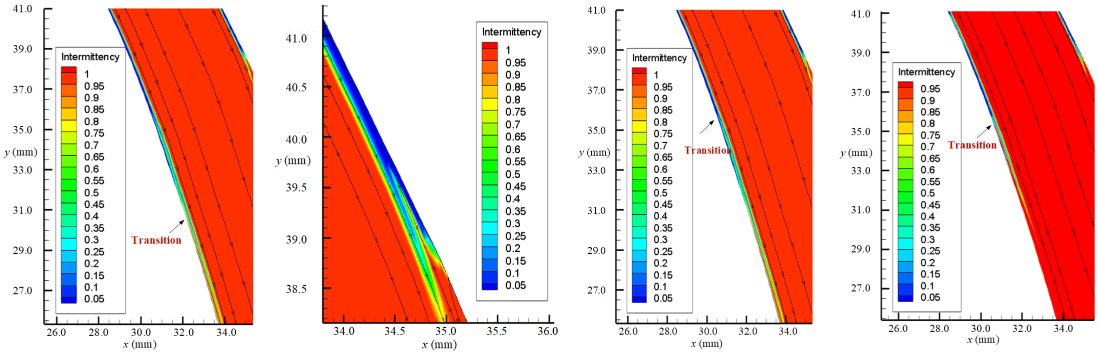


(a) Dry case with smooth blade (Suction side)

(b) Dry case with smooth blade (Pressure side)

(c) Wet case with smooth blade (Suction side)

(d) Wet case with roughness 10 μm (Suction side)

Fig. 31 Intermittency contour and streamline of transition flow near the suction side and pressure side with $p_{out}/p_{in}^{*} = 0.48$ in viscous dry and wet cases.

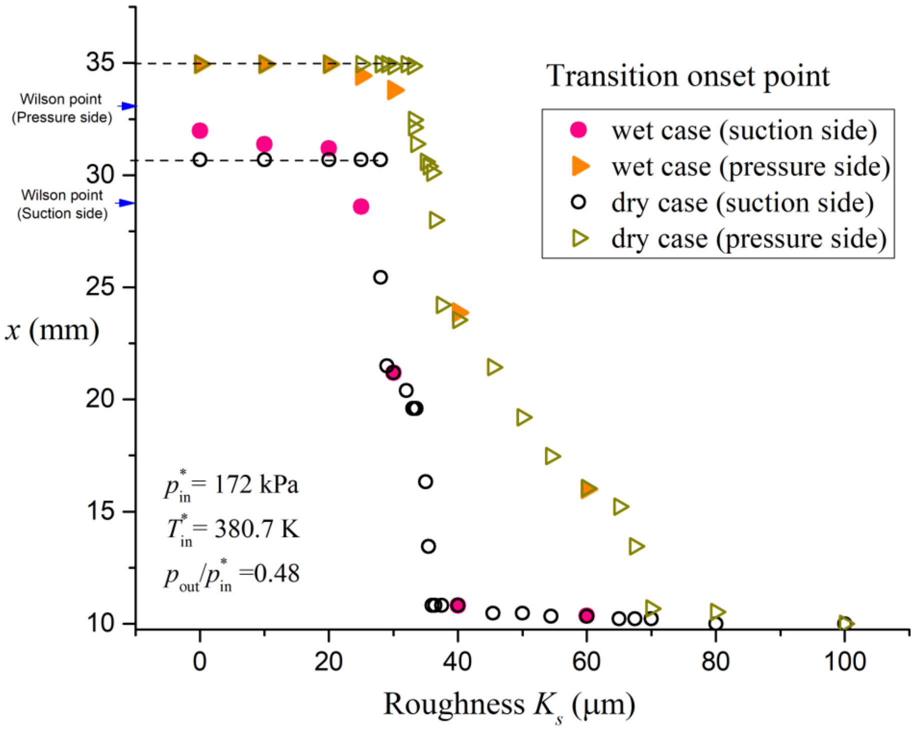


Fig. 32 The transition onset locations on the suction side and pressure side with $p_{out}/p_{in}^{*}$ = 0.48 in viscous dry and wet cases.

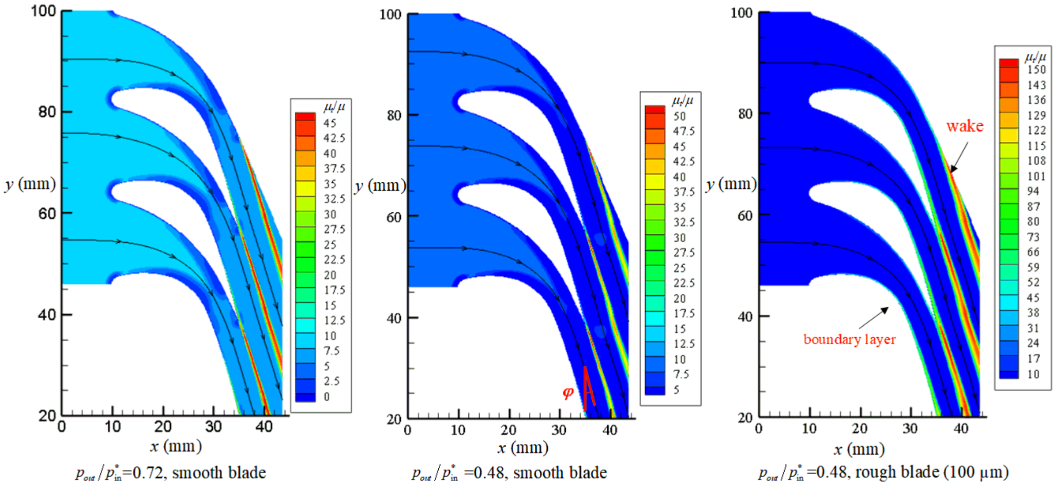


Fig. 33 The turbulent viscosity ratio contours in viscous wet cases.

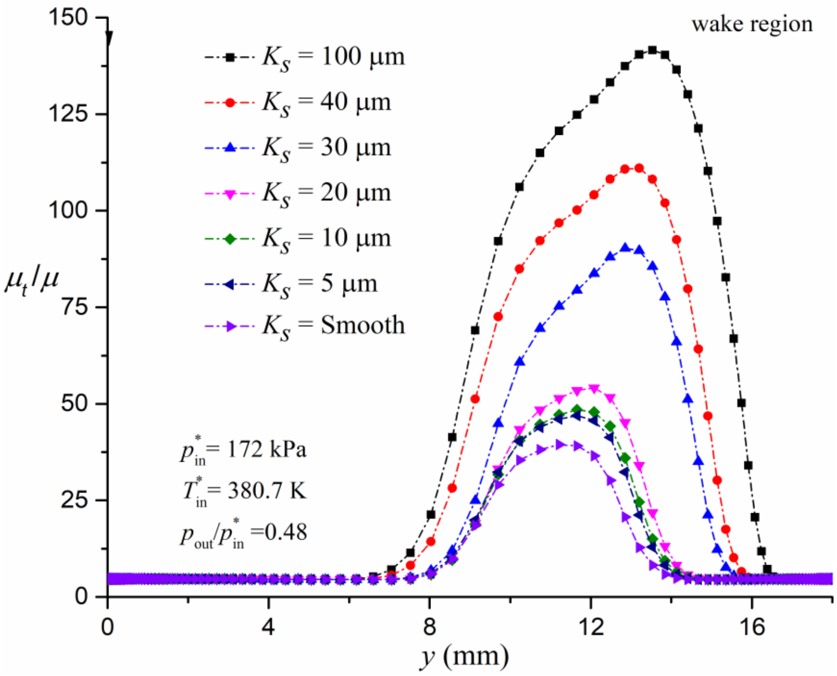

Fig. 34 The profiles of turbulent viscosity ratio at outlet with different roughness in viscous wet case.

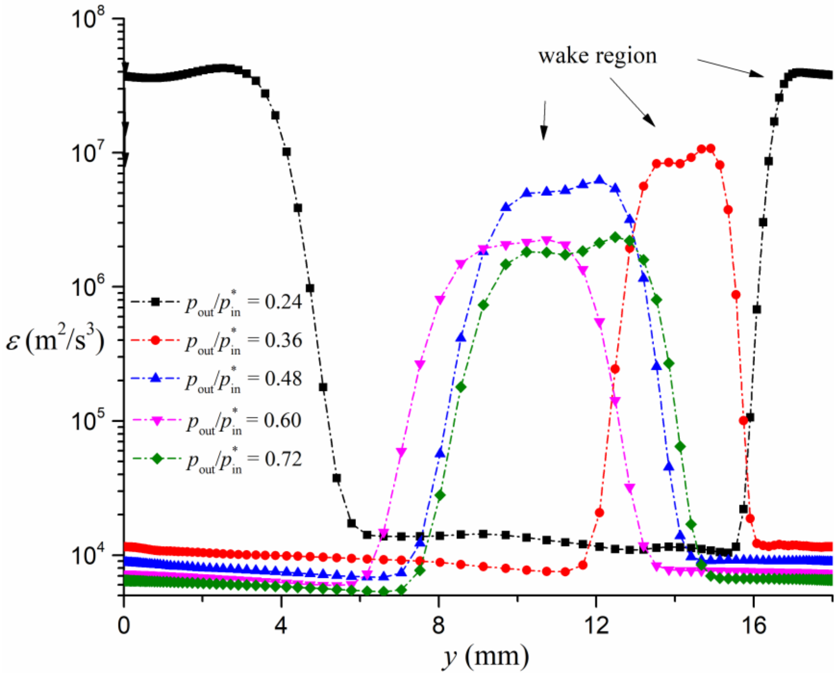


Fig. 35 The profiles of local turbulent dissipation rate at the outlet with different back pressure ratio $p_{out}/p_{in}^*$ for smooth blade in viscous wet case.

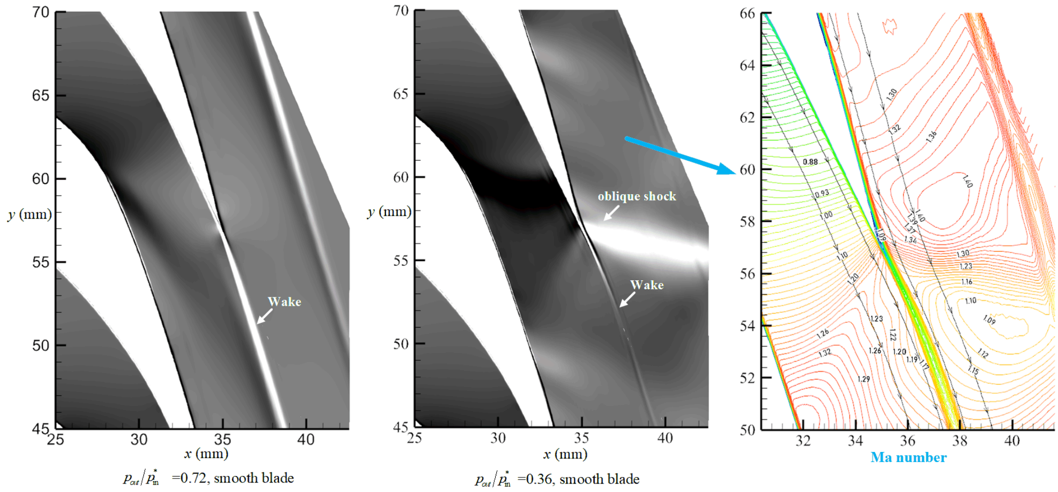


Fig. 36 Schlieren picture and Mach number contour with different back pressure ratio $p_{out}/p_{in}^{*}$ in viscous wet flow around the smooth blade.

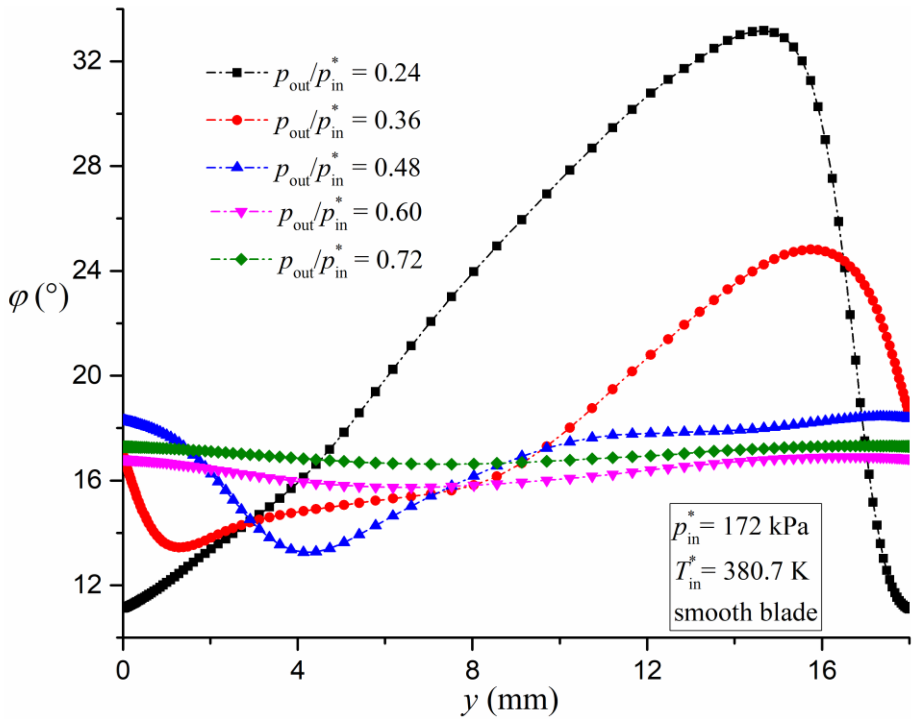


(a) different back pressure ratio $p_{out}/p_{in}^*$

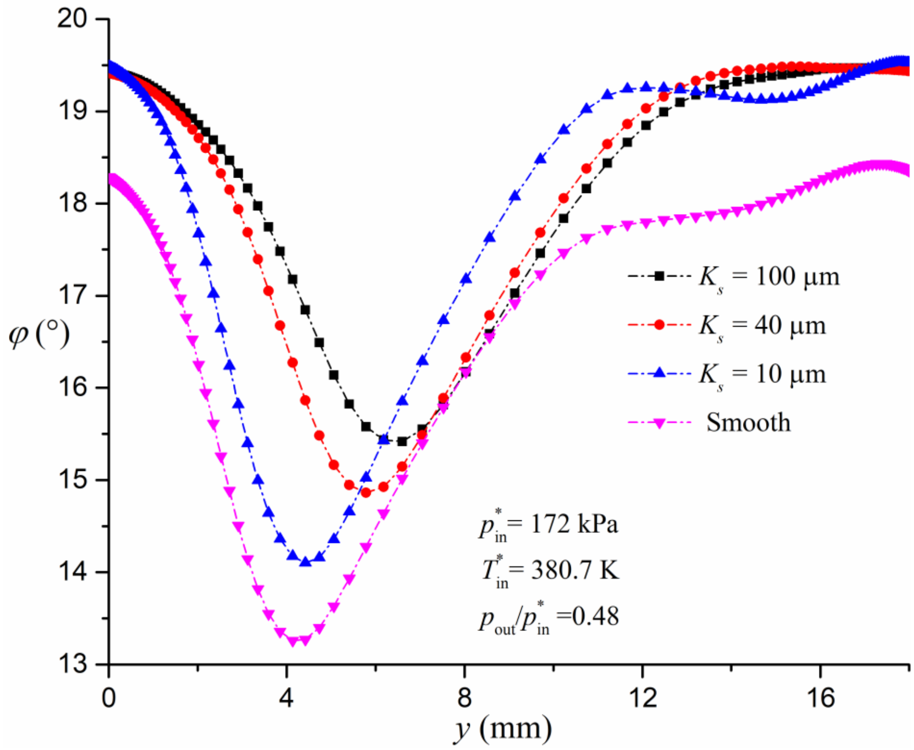


(b) different roughness $K_s$

Fig. 37 The profiles of local deviation angle at the outlet in viscous wet flow.

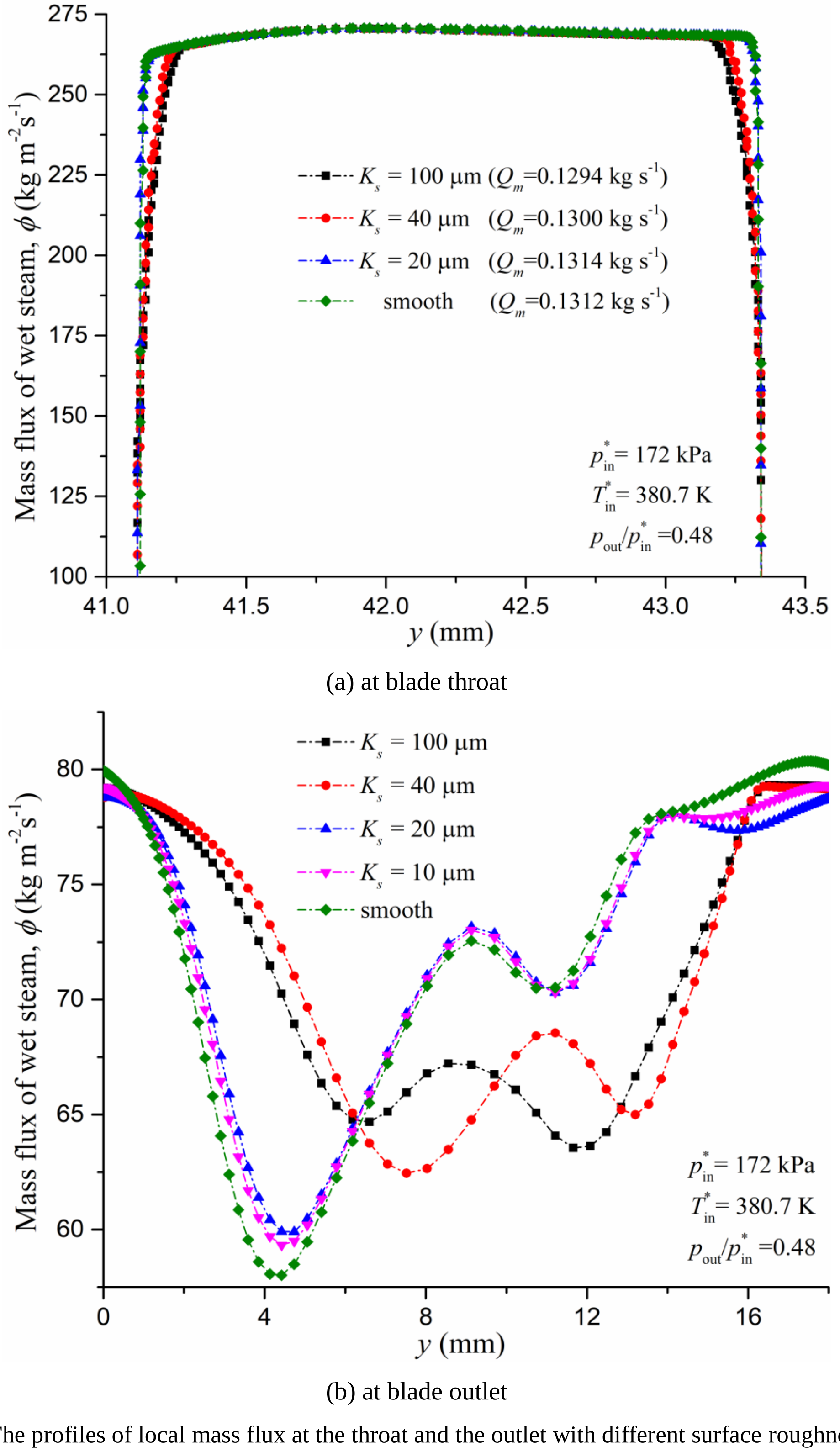


(a) at blade throat



(b) at blade outlet

Fig. 38 The profiles of local mass flux at the throat and the outlet with different surface roughness $K_s$ in viscous wet flow.

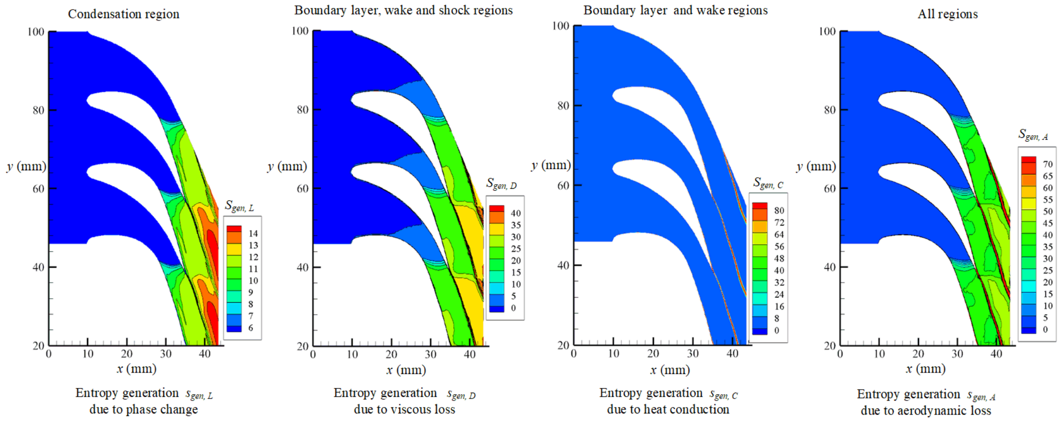


Fig. 39 The contours of various parts of entropy generation in viscous wet flow around the smooth blade with $p_{out}/p_{in}^*$ =0.36.

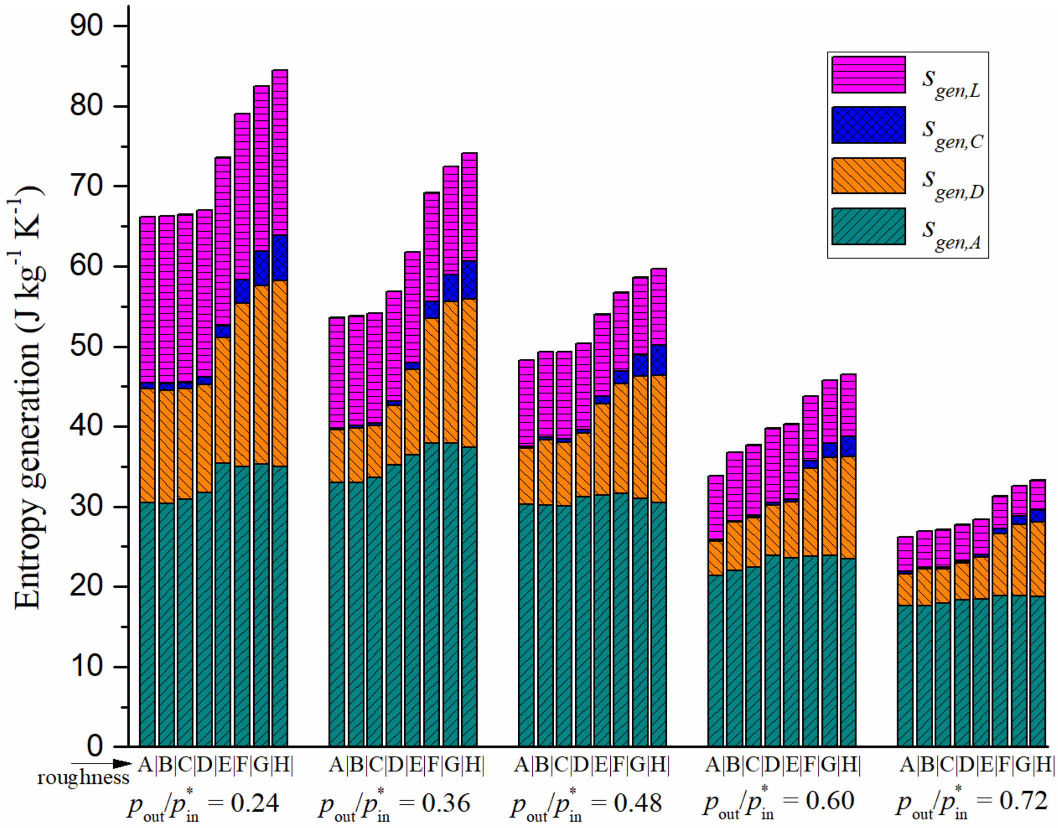


Fig. 40 The stacked column of mass-averaged entropy generations at the outlet in viscous wet flow with different roughness $K_s$ and back pressure ratio $p_{out}/p_{in}^*$.

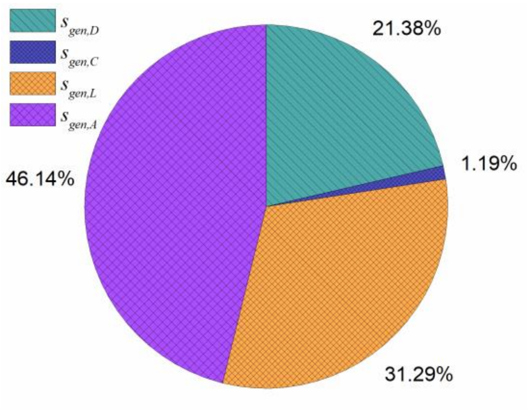


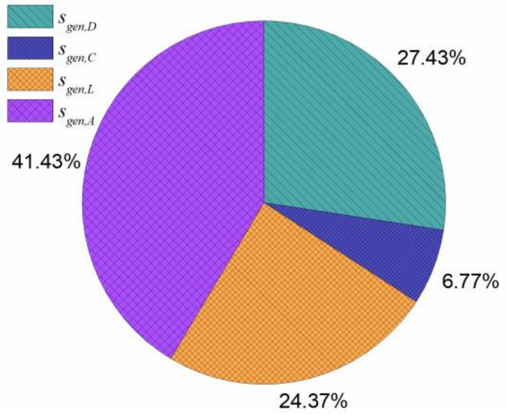


(a) $p_{out}/p_{in}^{*}$ = 0.24, smooth blade

(b) $p_{out}/p_{in}^{*}$ = 0.24, roughness 100 μm

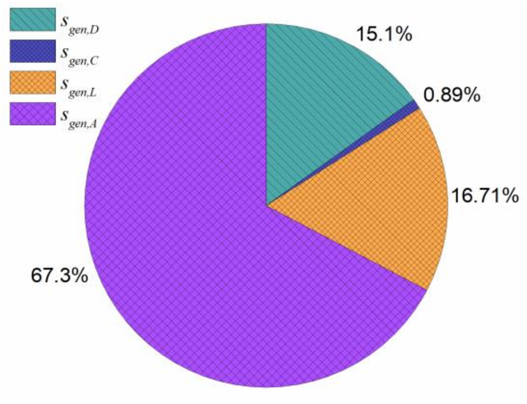


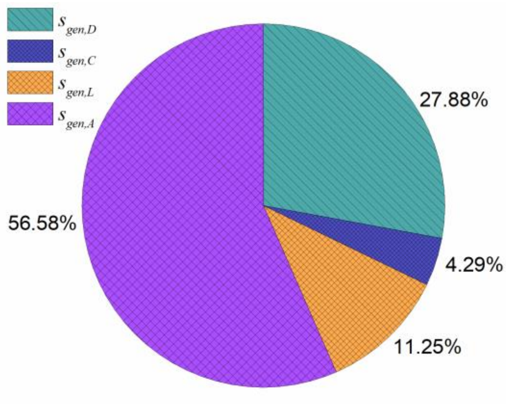


(c) $p_{out}/p_{in}^{*}$ = 0.72, smooth blade

(d) $p_{out}/p_{in}^{*}$ = 0.72, roughness 100 μm

Fig. 41 The percentages of each part of mass-averaged entropy generation at the outlet in viscous wet flow with different conditions.

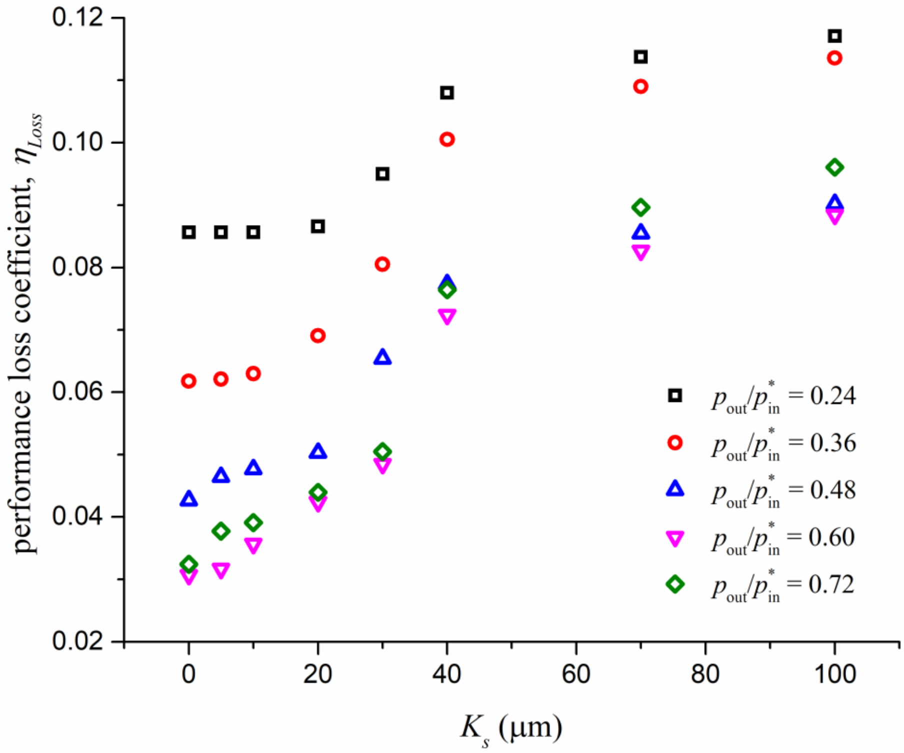


Fig. 42 The performance loss coefficient at the outlet in viscous wet flow with different roughness

$K_s$ and back pressure ratio $p_{\mathrm{out}}/p_{\mathrm{in}}^*$.

Table 8 The geometry sizes for the turbine blade cascade.

| Length | Chord | Pitch | Axial Chord | Inlet flow angle | width of chamber* |
|---|---|---|---|---|---|
| 76.00 mm | 35.76 mm | 18.26 mm | 25.27 mm | 0° | 100.00 mm |

Table 9 The mass-averaged wetness fraction $\beta_{avg}$ at the outlet with different roughness $K_s$ and back pressure ratio $p_{out}/p_{in}^*$.

| | Roughness | | | | | | | |
|---|---|---|---|---|---|---|---|---|
| $p_{out}/p_{in}^*$(-) | smooth | 5 μm | 10 μm | 20 μm | 30 μm | 40 μm | 70 μm | 100 μm |
| 0.24 | 0.05681 | 0.05651 | 0.05651 | 0.05644 | 0.05587 | 0.05482 | 0.05437 | 0.05407 |
| 0.36 | 0.04369 | 0.04367 | 0.04361 | 0.04324 | 0.04261 | 0.04152 | 0.04108 | 0.04085 |
| 0.48 | 0.03177 | 0.03166 | 0.03157 | 0.03143 | 0.03088 | 0.03042 | 0.03015 | 0.02997 |
| 0.60 | 0.02365 | 0.02332 | 0.02316 | 0.02299 | 0.02274 | 0.02225 | 0.02201 | 0.02182 |
| 0.72 | 0.01669 | 0.01676 | 0.01677 | 0.01668 | 0.01653 | 0.01579 | 0.01523 | 0.01495 |

Table 10 The mass-averaged deviation angle $\varphi_{avg}$ at the outlet with different roughness $K_s$ and back pressure ratio $p_{\mathrm{out}}/p_{\mathrm{in}}^*$.

| $p_{\mathrm{out}}/p_{\mathrm{in}}^*$(-) | Roughness | | | | | | | |
|---|---|---|---|---|---|---|---|---|
| | smooth | 5 µm | 10 µm | 20 µm | 30 µm | 40 µm | 70 µm | 100 µm |
| 0.24 | 25.177° | 25.191° | 25.197° | 25.257° | 25.508° | 25.544° | 25.603° | 25.642° |
| 0.36 | 18.975° | 18.988° | 19.001° | 19.055° | 19.122° | 19.054° | 19.072° | 19.085° |
| 0.48 | 16.828° | 16.854° | 16.877° | 16.904° | 16.969° | 16.971° | 17.006° | 17.034° |
| 0.60 | 16.336° | 16.476° | 16.530° | 16.610° | 16.667° | 16.731° | 16.797° | 16.838° |
| 0.72 | 16.974° | 17.101° | 17.171° | 17.234° | 17.277° | 17.238° | 17.271° | 17.300° |

Table 11 Each part of mass-averaged entropy generation ($J \cdot kg^{-1} \cdot K^{-1}$) at the outlet in viscous wet flow ($p_{out}/p_{in}^* = 0.36$) with different roughness $K_s$.

| Roughness | $s_{gen,\overline{D}}$ | $s_{gen,D'}$ | $s_{gen,\overline{C}}$ | $s_{gen,C'}$ | $s_{gen,L}$ | $s_{gen,A}$ | $s_{gen}$ |
|---|---|---|---|---|---|---|---|
| smooth | 4.412 | 2.144 | 0.185 | 0.093 | 13.738 | 33.002 | 53.573 |
| 5 μm | 4.621 | 2.172 | 0.183 | 0.109 | 13.710 | 32.994 | 53.790 |
| 10 μm | 4.457 | 2.060 | 0.181 | 0.128 | 13.718 | 33.645 | 54.189 |
| 20 μm | 4.332 | 3.045 | 0.198 | 0.317 | 13.758 | 35.241 | 56.891 |
| 30 μm | 4.432 | 6.221 | 0.265 | 0.636 | 13.784 | 36.432 | 61.770 |
| 40 μm | 4.861 | 10.714 | 0.518 | 1.558 | 13.594 | 37.920 | 69.166 |
| 70 μm | 5.689 | 11.982 | 1.079 | 2.244 | 13.518 | 37.932 | 72.443 |
| 100 μm | 6.161 | 12.406 | 1.639 | 3.065 | 13.461 | 37.392 | 74.124 |

Table 12 The mass-averaged entropy generations ($J \cdot kg^{-1} \cdot K^{-1}$) at the outlet in inviscid dry, viscous dry, viscous wet flows around the smooth blade with back pressure ratio $p_{out}/p_{in}^*$.

| $p_{out}/p_{in}^*$ | Conditions | $s_{gen,\overline{D}}$ | $s_{gen,D'}$ | $s_{gen,\overline{C}}$ | $s_{gen,C'}$ | $s_{gen,L}$ | $s_{gen,A}$ | $s_{gen}$ |
|---|---|---|---|---|---|---|---|---|
| 0.24 | Inviscid, dry | - | - | - | - | - | 19.008 | 19.008 |
| | Viscous, dry | 4.650 | 8.129 | 0.426 | 2.056 | - | 12.334 | 27.596 |
| | Viscous, wet | 5.003 | 9.150 | 0.249 | 0.540 | 20.707 | 30.536 | 66.185 |
| 0.36 | Inviscid, dry | - | - | - | - | - | 4.634 | 4.634 |
| | Viscous, dry | 4.841 | 2.831 | 0.321 | 0.768 | - | 8.134 | 16.895 |
| | Viscous, wet | 4.412 | 2.144 | 0.185 | 0.093 | 13.738 | 33.002 | 53.573 |
| 0.48 | Inviscid, dry | - | - | - | - | - | 9.735 | 9.735 |
| | Viscous, dry | 4.313 | 5.541 | 0.213 | 0.825 | - | 5.710 | 16.602 |
| | Viscous, wet | 3.997 | 2.939 | 0.134 | 0.142 | 10.772 | 30.310 | 48.295 |
| 0.60 | Inviscid, dry | - | - | - | - | - | 9.252 | 9.252 |
| | Viscous, dry | 3.584 | 5.899 | 0.150 | 0.641 | - | 2.899 | 13.173 |
| | Viscous, wet | 2.820 | 1.460 | 0.083 | 0.025 | 8.007 | 21.434 | 33.829 |
| 0.72 | Inviscid, dry | - | - | - | - | - | 0.389 | 0.389 |
| | Viscous, dry | 2.501 | 2.346 | 0.068 | 0.182 | - | 0.781 | 5.878 |
| | Viscous, wet | 2.325 | 1.638 | 0.056 | 0.178 | 4.386 | 17.664 | 26.248 |

Table 13 The total entropy generation ($J \cdot kg^{-1} \cdot K^{-1}$) at the outlet in viscous wet flow with different roughness $K_s$ and back pressure ratio $p_{out}/p_{in}^*$.

| $p_{out}/p_{in}^*$(-) | Roughness | | | | | | | |
|---|---|---|---|---|---|---|---|---|
| | smooth | 5 μm | 10 μm | 20 μm | 30 μm | 40 μm | 70 μm | 100 μm |
| 0.24 | 66.185 | 66.263 | 66.441 | 67.041 | 73.561 | 79.026 | 82.518 | 84.520 |
| 0.36 | 53.573 | 53.790 | 54.189 | 56.891 | 61.770 | 69.166 | 72.443 | 74.124 |
| 0.48 | 48.295 | 49.362 | 49.357 | 50.409 | 53.999 | 56.706 | 58.587 | 59.705 |
| 0.60 | 33.829 | 36.761 | 37.661 | 39.755 | 40.284 | 43.790 | 45.754 | 46.503 |
| 0.72 | 26.248 | 26.918 | 27.092 | 27.722 | 28.442 | 31.275 | 32.607 | 33.262 |

Table 14 The exergy destruction ratio $\zeta_D$ at the outlet with different roughness $K_s$ and back pressure ratio $p_{out}/p_{in}^*$.

| | Roughness | | | | | | | |
|---|---|---|---|---|---|---|---|---|
| $p_{out}/p_{in}^*$(-) | smooth | 5 μm | 10 μm | 20 μm | 30 μm | 40 μm | 70 μm | 100 μm |
| 0.24 | 0.0347 | 0.0347 | 0.0348 | 0.0351 | 0.0386 | 0.0414 | 0.0433 | 0.0443 |
| 0.36 | 0.0281 | 0.0282 | 0.0284 | 0.0298 | 0.0324 | 0.0363 | 0.0380 | 0.0389 |
| 0.48 | 0.0253 | 0.0259 | 0.0259 | 0.0264 | 0.0283 | 0.0297 | 0.0307 | 0.0313 |
| 0.60 | 0.0177 | 0.0193 | 0.0197 | 0.0208 | 0.0211 | 0.0230 | 0.0240 | 0.0244 |
| 0.72 | 0.0138 | 0.0141 | 0.0142 | 0.0145 | 0.0149 | 0.0164 | 0.0171 | 0.0174 |